

QSEG830 / PHYS646 LAB MANUAL  
COSMICWATCH:  
THE DESKTOP MUON DETECTOR (UD)

Contacts:

Prof. Spencer Axani ([saxani@udel.edu](mailto:saxani@udel.edu))  
Masooma Sarfraz ([masoomas@udel.edu](mailto:masoomas@udel.edu))  
Miles Garcia ([milesg@udel.edu](mailto:milesg@udel.edu))

March 7, 2024

# Contents

<b>1 DOCUMENT OVERVIEW</b>	<b>4</b>
<b>2 SOURCES OF IONIZING RADIATION</b>	<b>6</b>
2.1 Cosmic radiation . . . . .	6
2.1.1 Flux variations due to solar system properties . . . . .	10
2.1.2 Flux variations due to atmospheric properties . . . . .	11
2.2 Radioactive backgrounds . . . . .	12
<b>3 PARTICLE INTERACTIONS WITH MATTER</b>	<b>14</b>
3.1 High energy heavy charged particles . . . . .	14
3.2 High energy electrons/positrons and photons . . . . .	16
3.3 Low energy electrons/positrons . . . . .	17
3.4 Low energy gamma rays . . . . .	18
3.5 Neutrons . . . . .	19
<b>4 DETECTION METHODS</b>	<b>21</b>
4.1 Single Photon Detection: Photomultipliers . . . . .	21
4.2 Scintillators . . . . .	23
<b>5 THE COSMICWATCH DETECTOR</b>	<b>26</b>
5.1 Introduction to the Detector . . . . .	26
5.2 Recording data . . . . .	27
5.3 Setting detectors in master and coincidence mode . . . . .	29
5.4 What Can Possibly Go Wrong? . . . . .	31
<b>6 HOW TO BUILD A COSMICWATCH DETECTOR</b>	<b>34</b>
6.1 Overview . . . . .	34
6.1.1 Populating the PCB . . . . .	34
<b>7 TESTED MEASUREMENTS YOU CAN CHOOSE FROM</b>	<b>41</b>
7.1 Cosmic-ray Muon Angular Distribution . . . . .	42
7.2 Cosmic-ray muon attenuation in a Subway station . . . . .	43
7.3 Electromagnetic component of cosmic-ray showers . . . . .	44
7.4 Reducing radioactive backgrounds . . . . .	45

7.5	Correlation between the cosmic-ray muon rate and atmospheric pressure . . . . .	46
7.6	A true random number generator? . . . . .	48
7.7	Gamma-ray spectroscopy . . . . .	51
<b>8</b>	<b>UNTESTED MEASUREMENTS FOR THE ADVENTUROUS</b>	<b>52</b>
8.1	The velocity of cosmic-ray muons . . . . .	53
8.2	Muon Rate Underwater . . . . .	54
8.3	Muon lifetime . . . . .	55
8.4	Solar flares and the Forbush decrease . . . . .	56
8.5	Measuring the air shower size . . . . .	57
<b>9</b>	<b>FUN MEASUREMENTS WE HAVE DONE</b>	<b>59</b>
9.1	Measuring the cosmic-ray muon rate in an airplane at 33,000 ft . . . . .	59
9.2	High altitude balloon measurement at 107,000 ft . . . . .	60
9.3	Muon rate measurement while flying to the South Pole . . . . .	62
9.4	Latitude correction to the cosmic-ray muons . . . . .	64
9.5	Rate measurement 1 km underground at Super-Kamiokande . . . . .	66
9.6	Portable trigger system for an accelerator beamline . . . . .	68
<b>10</b>	<b>FUTURE MEASUREMENTS</b>	<b>69</b>
<b>11</b>	<b>PROGRAMMING THE MICRO-CONTROLLER</b>	<b>70</b>
11.1	Install Thonny . . . . .	71
<b>12</b>	<b>CONCLUSION</b>	<b>72</b>
<b>A</b>	<b>DESCRIPTION OF THE CIRCUIT</b>	<b>73</b>

# Chapter 1

## DOCUMENT OVERVIEW

This lab manual provides a comprehensive exploration of the physics associated with the v4 version of the CosmicWatch Desktop Muon Detectors. It commences by describing the types of ionizing radiation capable of triggering the detector. Subsequently, it delves into the impact of these radiation forms on the detector and their significance in our considerations.

The focus then shifts to details specific to the Desktop Muon Detectors, offering insights into the technology employed and the underlying physics. A section is dedicated to how we will also construct the detectors.

The latter portion of the document is dedicated to illustrating various physical phenomena discussed in earlier chapters through measurements conducted with the detectors. Along the way, intriguing facets of physics are briefly highlighted, aiming to inspire a deeper exploration beyond the scope covered here. As students generate new study ideas using this detector and analyze fresh data, these concluding chapters are envisioned to undergo continuous updates.

All material can be found in the GitHub repository located here:

<https://github.com/spenceraxani/CosmicWatch-Desktop-Muon-Detector-UD>

Numerous documents have played a crucial role in compiling this information. A great and valuable reference, both for the present and the future, is the Particle Data Group's (PDG) summary on cosmic rays [1] and energy loss in matter [2]. MIT Prof. Bruno Rossi's textbook, *Cosmic Rays* from 1964 [3], serves as an excellent entry-level resource, providing an early account of cosmic-ray physics investigations. It not only offers insightful reading but also allows readers to replicate many of the experiments conducted for the first time using the CosmicWatch detectors.

For a more contemporary perspective with a focus on history, Prof. Michael W. Friedlander's book titled *A Thin Cosmic Rain* [4] is recommended. Dr. Peter K. F. Grieder's comprehensive

textbook, *Cosmic Rays at Earth* [5], provides an in-depth overview of cosmic-ray physics and will be frequently referenced. In the realm of higher-energy cosmic-ray physics, Prof. Thomas K. Gaisser's book (from UD!!), *Cosmic Rays and Particle Physics* [6], proves to be extremely useful. Although Prof. Masataka Fukagita's two textbooks, *Physics of Neutrinos* and *Physics of Neutrinos and Applications to Astrophysics* [7], are primarily focused on the neutrino aspect, they often contain intriguing information not found in other readings.

For a comprehensive understanding of energy loss in matter, *Techniques for Nuclear and Particle Physics* by William R. Leo [8] stands out as the best resource for experimental particle physics. Additionally, Prof. Claus Grupen's textbook, *Particle Detectors* [9], is highly recommended as a reference for describing detection methods in particle physics.

The content of this lab manual has been lightly adapted from MIT's Junior Lab manual, which was based off of Prof. Spencer Axani's Masters Thesis, which can be accessed directly at <https://arxiv.org/abs/1908.00146>. However, this is a new detector, specifically designed for PHY646/QSEG830. We provide details on an upgraded detector, differing from the version in the thesis.

The CosmicWatch detector design has been developed with co-collaborator Dr. Katarzyna Frankiewicz and Prof. Janet Conrad. The original project has had funding from the MIT Physics Department, the Wisconsin Particle Astrophysics Center and the National Science Foundation, and is now funded through the University of Delaware.

We are excited to have the CosmicWatch detector incorporated into the experimental physics courses at UD! Developing this detector has been a passion, not just a hobby. We hope you enjoy it, and even consider building your own.

# Chapter 2

## SOURCES OF IONIZING RADIATION

Our discussion commences with an exploration of the diverse sources of ionizing radiation that can activate the Desktop Muon Detectors. Some forms of ionizing radiation hold particular significance due to their prevalence and energy levels. Additionally, we will touch upon why certain other forms of ionizing radiation do not register on our sensitivity, though a brief description of them is included for comprehensive understanding.

### 2.1 Cosmic radiation

The Earth experiences a continuous bombardment of particles known as *cosmic rays*. About 74% by mass of this cosmic-ray flux originates from ionized hydrogen (free protons), 18% from helium nuclei (two protons and two neutrons), and the remaining portion consists of trace amounts of heavier elements [1]. A significant fraction of the observed cosmic-ray flux at Earth is relativistic, meaning that the individual nuclei possess kinetic energies greater than their rest mass ( $E_k/mc^2 > 1$ ).

Lower energy cosmic-rays (GeV-scale) are significantly influenced by the solar wind and the Earth's geomagnetic field, as depicted in Fig. 2.1. These factors limit the flux interacting with the Earth. The high-energy flux extends up to  $10^{11}$  GeV, beyond which cosmic rays lose energy through interactions with the cosmic microwave background, known as the GZK cutoff<sup>1</sup>.

The energy of cosmic rays decreases rapidly: below  $10^6$  GeV, the flux decreases as  $E^{-2.7}$ , and above this, it steepens to approximately  $E^{-3.1}$  [6]. To provide perspective, the number of 1 GeV cosmic-ray protons is 8.1 orders of magnitude higher than that at 1000 GeV (i.e.,  $2.7 \times 3$ ), or

---

<sup>1</sup>The highest energy cosmic-ray observed, approximately  $3 \times 10^{20}$  eV [10] (48 joules), equivalent to a brick falling on your toe [11], was contained in a single proton and later named the *Oh-My-God Particle*.

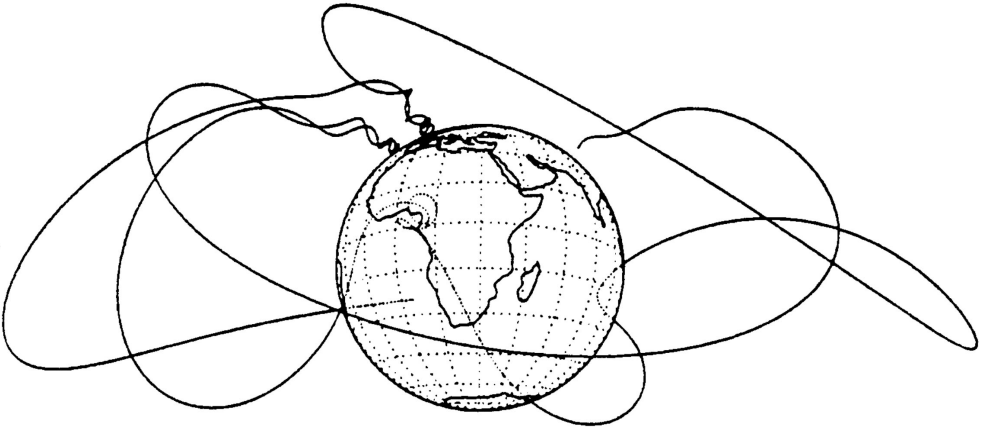


Figure 2.1: Simulated trajectories of low energy cosmic-rays interacting with the geomagnetic field. From Ref. [4]

16.2 orders of magnitude higher<sup>2</sup> than that at  $10^6$  GeV (i.e.,  $2.7 \times 6$ ).

When a primary cosmic-ray collides with a nucleus in the upper atmosphere (typically an oxygen or nitrogen nucleus), the energies involved can break apart either the primary particle or the target nucleus through nuclear interactions. The collision energy produces short-lived particles called *mesons*<sup>3</sup>. The most common mesons are the  $\pi$ -meson or pion ( $\pi^+, \pi^-, \pi^0$ ) and the K-meson or kaon ( $K^+, K^-, K^0$ ). Charged pions ( $\pi^\pm$ ) decay within approximately ten billionths of a second, producing muons and neutrinos (charged kaons,  $K^\pm$ , are more complex in their decay, but they also preferentially decay this way or to pions). Neutral mesons ( $\pi^0, K^0$ ) decay about one billion times faster ( $10^{-17}$ s) than charged mesons, primarily to gamma rays. Unlike neutral mesons, charged mesons can travel sufficiently before decaying to interact with another molecule in the atmosphere. This interaction may result in another nuclear interaction, similar to the primary cosmic-ray interaction, generating more mesons and contributing to the particle shower induced by the primary interaction.

Primary cosmic rays do not directly penetrate Earth's surface due to atmospheric shielding. However, a small flux of nuclear fragments (such as protons and neutrons) from these interactions can occasionally cascade down and reach the surface. Figure 2.2 illustrates a cosmic-ray interaction, with the initial interaction of vertical cosmic rays occurring at an altitude approximately between 15 and 20 km. Cosmic rays entering at an angle will interact at higher altitudes due to their path traversing more atmosphere [7].

The high energy photon from the decay of the neutral mesons quickly materialize into an

---

<sup>2</sup>The steep decrease in energy of the cosmic-ray flux necessitates large detectors for measuring rare high-energy events.

<sup>3</sup>Mesons, unlike protons and neutrons, contain only two quarks: one quark and one anti-quark. The lightest meson is the pion, followed by the kaon. Although there are many other quark/anti-quark pair combinations, their higher masses make them less preferentially produced and are not discussed here [12, 13].

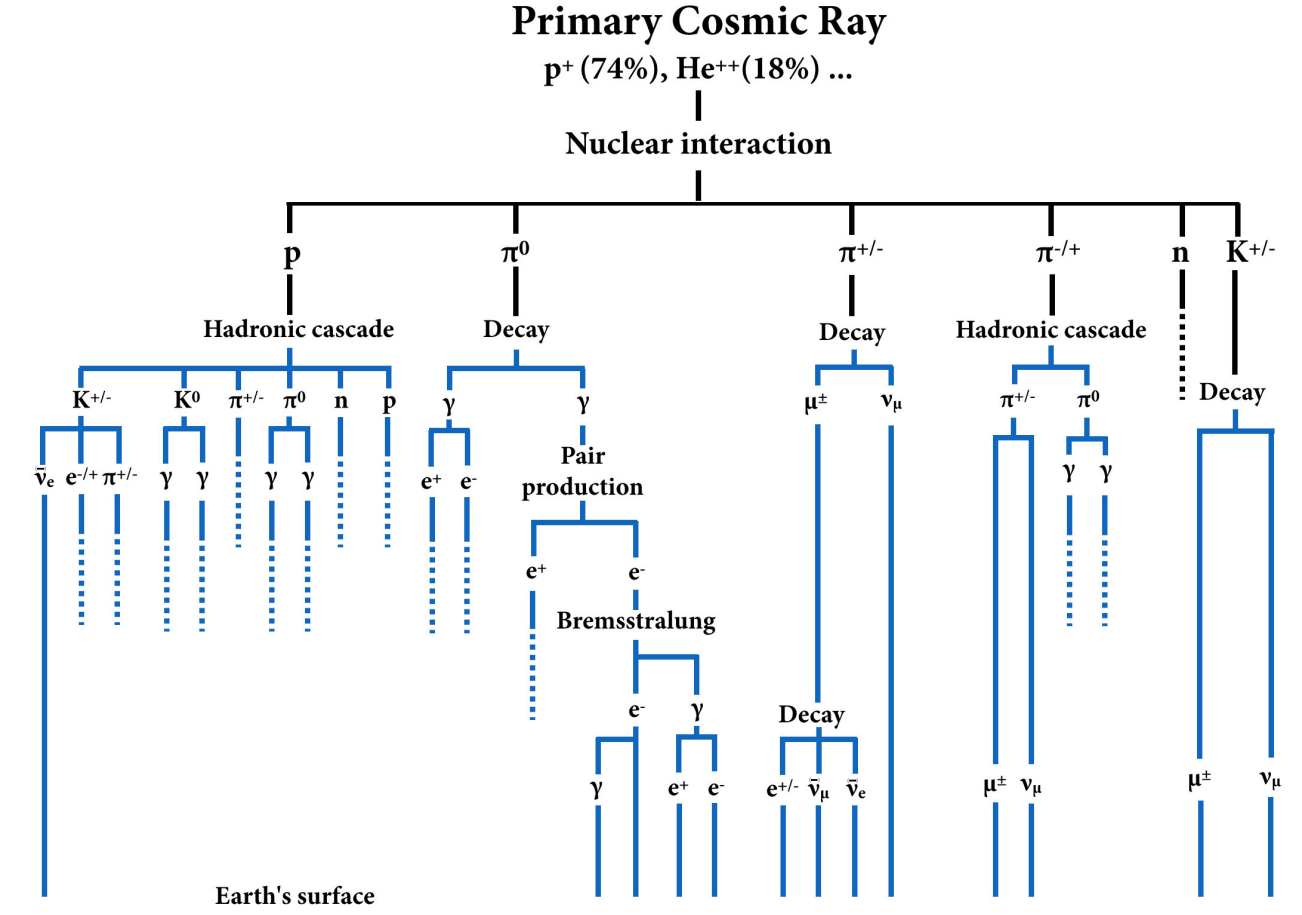


Figure 2.2: An schematic representation of the various decay and interactions chains that result from the interaction of a cosmic-ray in Earth’s atmosphere. This is a modified figure from Ref. [3].

electron-positron pair, also referred to as *pair production*. These electron-positron pairs then radiate high energy photons, which can again materialize into another electron-positron pair. This electromagnetic cascade process continues, dividing the original energy of the photons between the numerous electrons, positrons, and lower energy photons at the end of the cascade. Photons with energies less than 1.022 MeV cannot further pair produce and their interactions will be dominated by Compton scattering and photoelectric absorption. At lower altitudes, there isn’t a fresh supply of high energy neutral mesons due to the rapid decrease of nuclear interactions at lower altitudes.

The cosmic-ray muons ( $\mu^\pm$ ) originate from the decay of the charged mesons. A charged pion will decay to a same-sign muon (and muon-neutrino) with a branching fraction of 99.98%, whereas a charged kaon decays to a muon (and muon-neutrino) 63.5% of the time [14]. The neutrinos are not electrically charged and only interact through the weak force, therefore they can be fully ignored in this discussion.

$$\begin{aligned}\pi^\pm &\rightarrow \mu^\pm + \nu_\mu(\bar{\nu}_\mu) \dots (99.98\%) \\ K^\pm &\rightarrow \mu^\pm + \nu_\mu(\bar{\nu}_\mu) \dots (63.5\%) \end{aligned} \tag{2.1}$$

Approximately 80-90% of the muon flux in the energy range of interest (GeV to TeV-scale) comes from the decay of pions, and the remainder from kaons [15]. The muons are particularly penetrating, that is, they essentially only lose energy due to ionization as they travel through the atmosphere and other matter and can make it through a large amount of material. This is contrasted with *baryons* (particle comprised of quarks), which also interact through the strong force. This makes muons the most numerous charged particle showering down on the Earth's surface. Muons have a mass of 105.65 MeV and are also unstable particles with a half-life of  $2.2 \times 10^{-6}$ s. They decay to an electron and two neutrinos.

$$\mu^\pm \rightarrow e^\pm + \nu_e(\bar{\nu}_e) + \bar{\nu}_\mu(\nu_\mu) \dots (100.0\%), \tag{2.2}$$

however, again we can ignore the neutrinos. A cosmic-ray muon with an energy greater than 2.4 GeV will be sufficiently relativistic that its half-life, as seen by an observer on the Earth, will be dilated enough that it has a significant chance of reaching the Earth's surface before decaying. In other words, the muon decay length becomes greater than 15 km – the approximate altitude of the cosmic-ray muon production. Further, a typical muon will lose approximately 2 GeV of energy due to ionization as it passes through the atmosphere on its way to the ground. Combining these two facts with the fact that the geomagnetic field and interstellar solar winds drive back the GeV-scale cosmic-rays, as well as the steeply falling cosmic-ray energy spectrum, we can expect the average muon energy at Earth's surface to be greater than a few GeV. We typically quote the mean cosmic-ray muon energy at Earth's surface to be approximately 4 GeV [1]. The muons that do not survive the journey to the Earth's surface decay. The resulting electrons (or positrons in the case of a  $\mu^+$ ), also referred to as *Michelle electrons*, contribute to the low energy electromagnetic component from cosmic-ray showers at sea level.

Let us now compare the number of particles showering down on us at sea level. We'll limit ourselves to thinking about particles that are coming from one steradian about the zenith, this can be thought of as circular disk around the vertical (zenith) part of the sky whose area represents approximately  $1/6^{th}$  of the total visible sky, or equivalently, a half-angle of  $32^\circ$  from the zenith. From this direction, we can describe the number of particles passing through a  $1 \times 1 \text{ cm}^2$  horizontal surface per minute ( $\text{cm}^{-2} \text{ min}^{-1} \text{ sr}^{-1}$ ) by following the measurements outlined in Ref. [1]. We expect approximately  $0.4 \text{ cm}^{-2} \text{ min}^{-1} \text{ sr}^{-1}$  from  $\mu^\pm$  with energies greater than 1 GeV;  $0.2 \text{ e}^\pm \text{ cm}^{-2} \text{ min}^{-1} \text{ sr}^{-1}$  above 10 MeV, but the flux falls off fast with energy, becoming negligible above 1 GeV; and  $0.0054 \text{ cm}^{-2} \text{ min}^{-1} \text{ sr}^{-1}$  from protons above 1 GeV; and a charged meson flux above 1 GeV two orders of magnitude lower than that of the proton flux. This means that the protons and charged mesons are insignificant at sea level, however, there is a significant muonic and low-energy electromagnetic component. In Ref. [5], the flux is divided into a hard component (essentially fully muons), which can penetrate 15 cm of lead, and soft component (approximately 60-65% muons and the remainder is electrons, positrons, and photons), which cannot. As we'll soon see, there are a variety of physical phenomena that influence fluxes, but the relative contributions listed here represent a useful approximation.

As we increase in altitude, the relative contribution from the ionizing radiation fluxes change. In particular, we see a larger contribution from both the protons and electromagnetic component, whereas the charged mesons are still sub-dominant. Once we pass the primary interaction region where the primary cosmic-rays are most likely to interact (typically around 15-20 km), the secondary particles produced by the initial nuclear interaction die off and we see a decrease in the ionization radiation flux. The shape of the curve describing the ionizing radiation flux as a function of altitude is called the Pforzer curve, and where the ionizing particle production reaches a maximum is termed the Regener-Pforzer maximum [16].

### 2.1.1 Flux variations due to solar system properties

There are several properties associated with the interstellar medium that modulate the cosmic-ray flux, and in particular the observable cosmic-ray muon flux. These properties are primarily associated with behaviour of the Earth and Sun's magnetic field.

**The latitude effect:** Roughly speaking, the Earth has a magnetic field that behaves similarly to a magnetic dipole orientated from north to south. The magnetic field points parallel to the surface of the Earth near the equator, and perpendicular to the surface near the poles. Particles traveling towards the Earth will be less deflected ( $F=q\vec{v} \times \vec{B}$ ) near the poles compared to the equator. Low energy charged particles passing through the magnetic field may even become trapped in what's known as the *Van Allen radiation belt*. This presents a low energy cutoff, where the magnetic field is able to deflect protons below approximately 10 GeV near the equator (corresponding to a rigidity of 10 GV) and near 1 GeV at higher latitudes [17, 18].

**The East-West asymmetry:** The cosmic-ray muon flux is larger looking towards the west compared to the east due to the Earth's magnetic field. This is an effect produced by primary cosmic-ray particles being predominately positively charged. The positively charged muons curve towards the east, meaning that the intensity from the west is stronger. This effect is more evident in the upper atmosphere [5], and obviously a larger effect at the geomagnetic equator than at the poles.

**Magnetic anomalies:** There are local geomagnetic field variations, which causes a change in the cosmic-ray intensity. The most prominent being the *South Atlantic Anomaly (SAA)* [19], which extends from the east coast Brazil to the west coast of southern Africa (-50.0 to 0.0 geographic latitude and from -90.0 to 40.0 longitude). This is the region where Earth's inner Van Allen radiation belt extends closest to the planet's surface and provides the smallest amount of protection from cosmic-rays. In fact, the increased level of ionizing radiation when passing through the SAA is responsible for radiation damage to electronics on-board Low-Earth Orbit (LEO) satellites<sup>4</sup>.

---

<sup>4</sup>The International Space Station (ISS) passes intermittently through the SAA [20] and has dedicated instrumentation for measuring the increased radiation dose to astronauts [21]. Astronauts from NASA missions as early as Apollo 11 [22] have also reported seeing flashes of light while being in orbit [23]. These flashes of light are attributed to high-energy particles in the space radiation environment, however many details on the origin

**Solar modulation:** The observed cosmic-ray flux at the top of the Earth’s atmosphere depends partially on solar activity, which manifests itself as an 11-year cycle<sup>5</sup>. Solar winds can drive back low energy cosmic-rays entering the solar sphere and the modulation effect decreases with an increase in energy. According to Ref. [7], the 1 GeV cosmic-ray proton flux is twice as small during maximum solar activity compared to minimum solar activity; similarly there is a 10% reduction in the 10 GeV cosmic-ray protons during the solar maximum.

**Solar Flares:** Solar-flares can eject protons with energies up to several GeV, the upper end of which is able to produce muons through nuclear interactions. These events are rare transients, and since the energy is low, it primarily has an effect on the low energy muon flux [25].

### 2.1.2 Flux variations due to atmospheric properties

Similar to the previous subsection, there exists terrestrial phenomena that also modulate the cosmic-ray muon flux.

**The Cosine Squared Law:** At greater angles from the vertical, cosmic-ray muons must travel through a much larger distance, and therefore amount of matter, to reach a ground-based observer. A cosmic-ray muon traveling vertically downwards may only travel through 15 km of atmosphere, whereas one traveling in the horizontal direction must pass through approximately 500 km of atmosphere. The larger path length means that the muon will lose more total energy due to ionization in the atmosphere and also have a higher probability of decaying before reaching the ground. As a function of zenith angle, the cosmic-ray muon intensity is expected to follow a cosine squared dependence [1].

**The atmospheric attenuation:** Recall that the nuclear interactions between the primary cosmic-ray and atmospheric nucleus happen in the upper atmosphere. Therefore, particles reaching sea level must have had sufficient energy to penetrate the remainder of the atmosphere. An increase in atmospheric density (perhaps due to atmospheric pressure changes) will cause secondary particles to lose more energy as they propagate to the Earth’s surface. Due to this, the muon rate turns out to be anti-correlated with the pressure (i.e. if the atmospheric pressure increases, the cosmic-ray muon rate decreases). The density of the atmosphere changes with the season and therefore exhibits a time-dependence. From other measurements, this is expected to be a percent level effect [26].

**The positive temperature effect:** To produce a muon, we require a charged meson to decay. However, recall that the charged mesons are typically relativistic and have lifetimes on the order of nanoseconds<sup>6</sup>. This gives the charged mesons sufficient time to potentially interact

are still unknown [24]

<sup>5</sup>There is also a 22-year cycle since the solar magnetic dipole flips polarity at every solar maximum, which occurs every 22 years [5]

<sup>6</sup>For example, a 5-GeV  $\pi^\pm$  produced at 15 km will travel approximately 300 m before decaying. This distance is small compared to the interaction path length of approximately 13 km, which means that most charged pions

with another nucleus in the atmosphere rather than decay. As the temperature increases, the atmosphere expands and there are fewer particles to interact with, thus increasing the probability of decaying rather than interacting [27].

Rather than correlating this with the ground based pressure (as in the paragraph above), it is more commonly correlated with atmospheric temperature – taking into account the temperature profile of the atmosphere. This effect is larger at higher energies and therefore is typically measured in laboratories located deep underground where the low energy cosmic-rays have less of an influence [28–30].

**The negative temperature effect:** As the temperature of the atmosphere increases, the atmosphere expands, moving the muon production region further out. This means that the muon path length increases, which gives them a higher probability of decay prior to making it to the ground. During the winter when the atmosphere is colder, shallower and more dense, cosmic-ray interactions happen closer to the Earth’s surface. The charged mesons quickly begin to lose energy and have a less likely chance of decaying into muons.

## 2.2 Radioactive backgrounds

The previous section described the ionizing radiation that we expect from showers of particles raining down from the upper atmosphere, and the expected phenomena that can modulate this flux. This section will describe ionizing radiation that originates on the surface of Earth and can also influence our measurements; we’ll refer to these as the *radioactive backgrounds*. Radioactive backgrounds are sub-divided into primarily three main processes called alpha, beta, and gamma radiation. Radioactivity is a quantum mechanical effect, which is non-deterministic, that is, we cannot predict when a particle will decay, rather we can only assign a probability to it. The energy scale of these processes are relatively low (MeV-scale) compared to the energies associated with the cosmic-rays (GeV and above), but their natural abundance on the surface of the Earth is sufficient that these are typically the dominant source of triggers in the Desktop Muon Detector.

Alpha decay is the result of an unstable nucleus ejecting a helium nucleus (a bound state of two protons and two neutrons),  $(Z, A) \rightarrow (Z - 2, A - 4) + \alpha$ . This is a quantum mechanical effect, where a helium state (helium is a very tightly bound state) forms in the nucleus, then quantum tunnels through the nuclear potential barrier, exiting the nucleus. The emitted alpha particle is mono-energetic, and since the helium nucleus has a charge of  $+2e$  and mass of approximately 4 GeV (therefore, it moves slow and has a large charge), it will lose energy rapidly in matter. A 5-MeV alpha particle will have a range of 3.5 cm in air before losing all of its energy, or equivalently, 23 micrometers in aluminum<sup>7</sup> [31].

---

will decay rather than interact. However, at approximately 115 GeV, the pion has an equal probability to interact or decay in the atmosphere.

<sup>7</sup>The high energy loss rate that alpha radiation makes it useful for cancer therapies. An alpha particle will

Beta radiation is described as the decay of a neutron to a proton<sup>8</sup>:  $n \rightarrow p + e^- + \bar{\nu}_e$ . The proton remains in the nucleus, while the electron and electron-neutrino are ejected. Since this is a 3-body decay, the electron is not mono-energetic. It is emitted with a continuous energy spectrum whose maximum energy is approximately at the total energy available for the decay (the Q-value). Beta decays typically have energies that can range from tens of keV to a few MeV.

Gamma radiation is simply a high-energy photon, emitted during the de-excitation of an atomic nucleus. When the nucleus is in an unstable state (for example, maybe the nucleus absorbed a neutron or was left in an excited state after a beta decay), it will de-excite into a lower energy configuration releasing a photon. This is analogous to the de-excitation of an atomic electron, emitting a characteristic mono-energetic photon. Since the energy levels in the nucleus are quantized, gamma ray are also mono-energetic (with a small spread due to nuclear motion). These energy scales are in the 100 keV to MeV-range.

---

deposit all of its kinetic energy into a very local space (order micrometers in human tissue), which is capable of destroying cancerous cells.

<sup>8</sup>More fundamentally, during neutron decays, a down-quark in the neutron converts to a up-quark, emitting a virtual W-Boson  $u \rightarrow d + W \rightarrow d + e^- + \bar{\nu}_e$ . On the macroscopic level, this appears as the transmutation of an atom converting to another atom with an extra proton and one fewer neutron:  $A(Z, N) \rightarrow A'(Z + 1, N - 1) + e^- + \bar{\nu}_e$ .

# Chapter 3

## PARTICLE INTERACTIONS WITH MATTER

To identify a particle, it is essential for it to engage in an interaction with the detector's material, facilitating the transfer of energy from the particle to the absorbing substance. This segment will delve into the primary interactions that effectively transmit energy from particles like muons, protons, pions/kaons, and other high-energy heavy charged particles. Subsequently, we will explore interactions related to high-energy electrons (including positrons) and conclude with those associated with radioactive backgrounds.

### 3.1 High energy heavy charged particles

The following explanation proves valuable when considering any charged particles with a mass significantly greater than that of the electron ( $m \gg m_e$ ). This encompasses all charged particles except for the electron and positron. For instance, the muon, the next lightest charged particle, is 206 times more massive than the electron. In contrast to the linear trajectories of heavy charged particles, electrons do not follow straight paths within a target, necessitating special consideration. The description provided below offers an approximation of the fundamental processes contributing to energy loss in matter, acknowledging that the scope of this topic is too extensive to cover comprehensively in a single document. More information can be found in Ref. [2, 9, 32, 33].

The rate of energy loss, often denoted as stopping power ( $-dE/dx$ ), quantifies the amount of energy lost per unit distance traveled. It is commonly measured in units of MeV cm<sup>2</sup>/g, known as *mass stopping power*. To obtain the energy lost per centimeter, one simply multiplies this value by the density (in g/cm<sup>3</sup>) of the material being traversed. To facilitate comparisons, we express the energy loss rate in terms of water ( $\rho = 1.0 \text{ g/cm}^3$ ), which conveniently shares a similar density with plastic scintillator. As a particle moves through a substance, its energy loss can be categorized into three mass-dependent ranges:

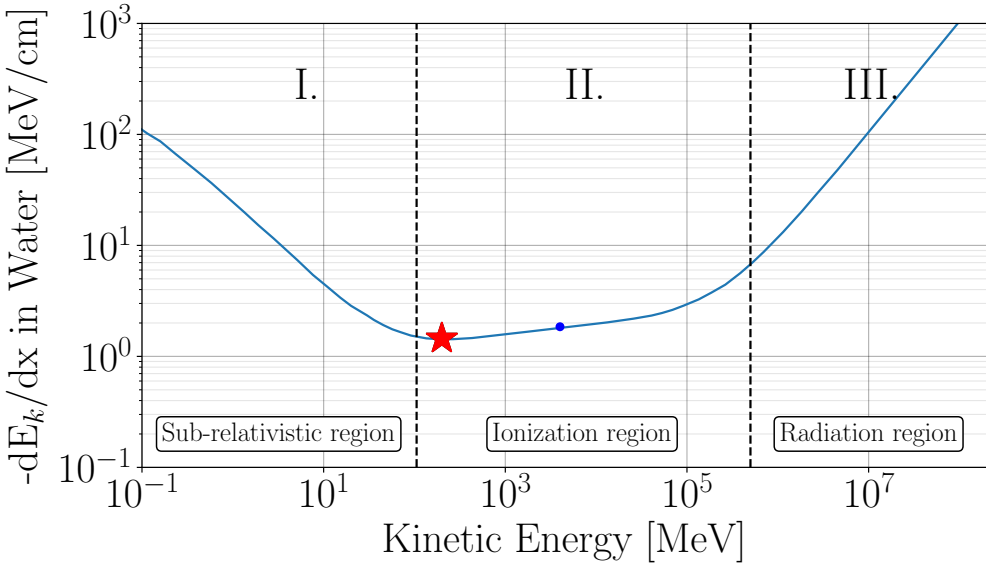


Figure 3.1: The kinetic energy loss per centimeter traveled, of a muon traveling through  $\text{H}_2\text{O}$  ( $\rho = 1.0 \text{ g/cm}^3$ ). Modified from Ref. [34]. The blue dot represents the mean energy of the cosmic-ray muons at sea level (4 GeV), and the red star represents where the particle is minimally ionizing.

- I. The sub-relativistic region: ( $E_k < mc^2$ )
- II. The ionization region: ( $E_k > mc^2$  and  $E < 400 \text{ GeV m}^2/\text{m}_{\mu}^2$ )
- III. The radiation region ( $E > 400 \text{ GeV m}^2/\text{m}_{\mu}^2$ ).

The delineation of these three regions is depicted in Fig.3.1 for a muon traversing water. However, the energy loss can be adapted to another material by straightforwardly multiplying it by the density (in  $\text{g/cm}^3$ ) of that material. For instance, the stopping power in lead would be adjusted by a factor of 11.34. Similarly, the energy loss can be tailored to a different particle by multiplying it by the square of the particle's charge. For instance, the energy loss of an alpha particle would be scaled by a factor of 4. While this plot is commonly presented in terms of momentum, we have scaled it using the kinetic energy of the incident particle for simplicity in explanation. The vertical dashed lines, marking the boundaries of the three regions, can be adapted to another charged particle using the aforementioned principles. For instance, a proton would enter the sub-relativistic region at approximately 1GeV.

In the **sub-relativistic region** (Muon:  $E_k \approx 100 \text{ MeV}$ ; Proton:  $E_k \approx 1 \text{ GeV}$ ), As the particle loses energy, the rate of energy loss per unit distance traveled increases. Essentially, this implies that once a particle enters this region, it rapidly decelerates and comes to a stop quickly. This phenomena is also known as the *Bragg peak* [8].

In the **high energy radiation region** (Muon:  $E_k \approx 400 \text{ GeV}$ ; Proton:  $E_k \approx 27 \text{ TeV}$ ), the

energy loss is associated with *bremsstrahlung*, pair production, and nuclear interactions, and scales linearly with energy. The radiation term becomes predominant at around 400 GeV for muons. However, it's important to note that the cosmic-ray flux decreases rapidly with energy. Muons in this energy regime constitute only a small percentage of the overall flux and experience rapid energy loss.

Finally, the **ionization region** encompasses the majority of the cosmic-ray muon flux. It is noteworthy that the mean muon energy at sea level is 4GeV, as indicated by a blue marker in Fig.3.1. The energy loss in this region results from ionization (breaking electromagnetic bonds) and excitation (raising the electron to a higher-lying shell within the absorber atom) of the incident particle. This behavior is described by the *Bethe Bloch formula*. Detailed explanations of the formula can be found in Refs. [8,9,34]).

This region is particularly fascinating because the energy loss rate remains nearly constant (increasing logarithmically), with an average energy loss rate of 2.2MeV/cm in a material with a density of 1.0g/cm<sup>3</sup> across many orders of magnitude. The minimum point, denoted by a red star in Fig.3.1, designates the muon as a minimum ionizing particle (MIP), representing the energy at which the muon is most penetrating. The function exhibits such a flat trend in the vicinity of this minimum (up to approximately 400GeV) that any particle with energy near this red star is commonly referred to as a MIP. Interestingly, the majority of the cosmic-ray flux falls within this region. Consequently, to estimate the penetrating depth of a typical cosmic-ray muon, one can simply divide the energy by 2.2MeV/cm and multiply by the density of the absorber. For instance, a 10GeV muon can penetrate through approximately 17m of concrete (= 2.7g/cm<sup>3</sup>).

As for other heavy charged particles discussed in this document—protons, pions, and kaons—they also lose energy through ionization. However, due to their composition of quarks, they can also interact via the strong force. The strong force is responsible for nuclear collisions that can significantly impact the particle and its trajectory. This unique property makes muons stand out—they do not interact via the strong nuclear force, and being heavy allows them to penetrate through materials with minimal losses due to collisions with electrons in the absorbers and with minimal deflection in their trajectory<sup>1</sup>.

## 3.2 High energy electrons/positrons and photons

As discussed in Section 2.1, a notable source of electrons/positrons with energies below 1 GeV showers onto the Earth's surface. This section focuses on describing the energy loss for high-

---

<sup>1</sup>Given their ability to penetrate very large distances through materials, many experiments are situated kilometers underground to shield against high-energy muons. For example, the neutrino detector Super-Kamiokande is buried underneath a 1-km mountain in Japan to reduce the muon flux by a factor of  $10^5$ , preventing them from overwhelming the search for rare, less energetic interactions from neutrinos. Similarly, the IceCube neutrino detector is buried under 1.4 km of ice in the Antarctic glacier at the South Pole for similar reasons.

energy electrons, with the understanding that the explanation is equally applicable to positrons. For electrons above a few tens of MeV, radiation losses, primarily through *bremsstrahlung radiation* (translated as "braking radiation" in German), dominate the energy loss mechanism. Bremsstrahlung radiation involves the emission of photons when a particle accelerates and decelerates in the vicinity of the electric field of the material's nucleus.

A bremsstrahlung photon with sufficient energy can undergo pair production, yielding an electron and positron, which subsequently emit additional bremsstrahlung photons, initiating a cascade of electrons, positrons, and photons. This process governs the energy loss of the electron until its energy drops below a few tens of MeV, commonly referred to as the critical energy. Remarkably, the radiation energy loss rate scales with energy. In the region above the critical energy, the rate of energy loss ( $dE/dx$ ) is proportional to the energy. Consequently, a 20GeV electron, for instance, initially loses energy per centimeter traveled at a rate 1000 times greater than a 20MeV electron, predominantly through bremsstrahlung radiation. This leads to a rapid decrease in the energy of high-energy particles as a function of distance traveled.

A *radiation length*, denoted as  $X_0$ , is defined as the average thickness of a material that reduces the mean energy of an electron or positron by a factor of  $1/e$  (Euler's number = 2.71828) due to bremsstrahlung radiation. In practical terms, this implies that an electron will lose a factor of  $e^{-t}$  energy after traversing  $t$  radiation lengths. For instance, after four radiation lengths, a 1 GeV electron will end up with approximately 20 MeV. The simplified *Heitler Model for electromagnetic cascades* approximates this by stating that one electron-positron pair will be created per radiation length, and each pair will receive half of the energy of the photon that produced them. After  $t$  radiation lengths, the cascade will contain  $2^t$  particles (electrons, positrons, and photons), each with an average energy of approximately  $E = \frac{E_0}{2^t}$  [35]. This concept is illustrated in Fig. 3.2.

A valuable list of radiation lengths for various materials is provided in Table 3.1. This table includes information about materials relevant to the Desktop Muon Detectors or used in some measurements below.

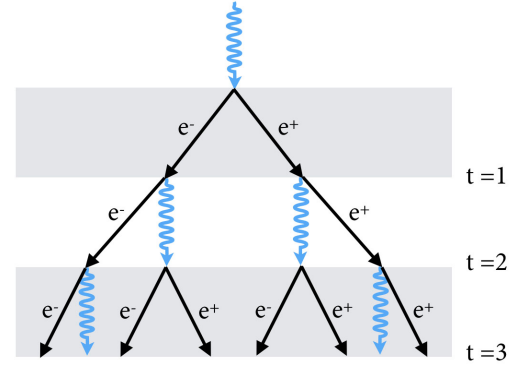


Figure 3.2: The Heitler Model for electromagnetic cascades.

### 3.3 Low energy electrons/positrons

Electrons and positrons, being the lightest charged particles, exhibit qualitative behavior in electron scattering distinct from that of high-energy particles in two ways. Firstly, the energy

Material	Density [g/cm <sup>3</sup> ]	Radiation length [cm]	Critical Energy [MeV]
Water (H <sub>2</sub> O)	1.00	36.1	92
Lead (Pb)	11.35	0.56	9.51
Concrete	2.5	10.7	
Air at STP*	1.2931	30420	102
Scintillator (Polystyrene)	1.032	42.4	109
Aluminium (Al)	2.70	8.9	51.0

Table 3.1: A table of materials that are mentioned in this document and their corresponding radiation length. \*STP indicates that the air is at the standard temperature and pressure: 20°C and 101.325 kPa. The data was collected from Ref. [1,8].

loss by electrons fluctuates significantly more than that of heavy particles. For instance, the maximum transferable kinetic energy of a 4 GeV electron is the full 4 GeV (given their equal masses), whereas a muon with the same energy has a maximum transferable energy of approximately 1 GeV. Secondly, due to their small mass, electrons are particularly prone to experiencing large-angle deflections when scattering off a nucleus. This susceptibility is so pronounced that multiply scattered electrons may undergo a complete reversal in direction, a phenomenon defined as *backscattering*. The probability of backscattering is higher at lower energies, and if backscattered, electrons do not deposit all their energy in the absorbing medium. For instance, a 1 MeV electron has approximately a 10% chance of backscattering off a thick slab of aluminum, and a 50% chance of backscattering off a slab of gold. [36].

The previous section described electrons and positrons with energy above the critical energy of a material (typically tens of MeV), where their energy loss is completely dominated by bremsstrahlung radiation. At lower energies, electrons and positrons can inelastically interact through Coulomb collisions with atomic electrons to lose energy [37]. This leads to ionization and excitation, similar to the behavior observed in heavier particles. At even lower energies, in the MeV scale, electrons (positrons) also exhibit *Møller (Bhabha)* scattering.

### 3.4 Low energy gamma rays

Gamma-rays interact slightly differently from the charged particles due to their lack of electric charge. The three main interactions of gamma rays (and X-rays) are shown in Fig. 3.3.

An atomic electron can fully absorb the energy of a gamma ray<sup>2</sup>, resulting in an electron with the energy of the initial gamma ray (MeV-scale) minus the binding energy of the atomic electron (eV-scale). This process is known as the *photoelectric effect*. As shown in Fig. 3.4, the photoelectric effect dominates for low-energy gamma-rays with a moderate-to-high density absorber.

---

<sup>2</sup>In order to conserve momentum, the photoelectric effect cannot occur on a free electron; it requires a nucleus to absorb part of the recoil.

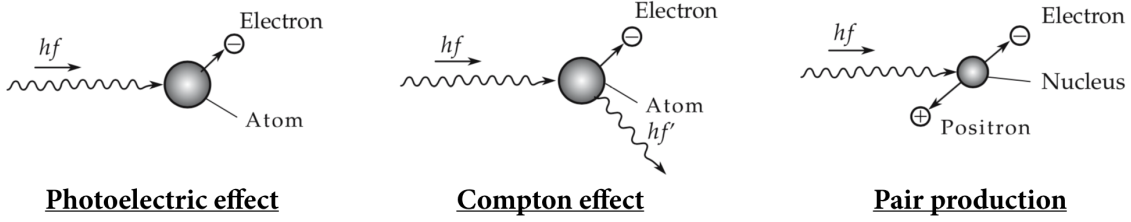


Figure 3.3: Modified from Ref. [31]

*Compton scattering* involves the partial transfer of energy from the incident gamma-ray to an atomic electron, leading to the electron's elevation to a higher energy level or ionization. The gamma-ray may alter its direction, exiting the material containing the electron, or it might undergo further scattering with another electron. Compton scattering prevails at low energy for materials with very low atomic numbers ( $Z$ ), and the likelihood of scattering is directly proportional to the electron density, and thus, to the proton number of the material.

At energies above 1.022 MeV, electron-positron pair production plays a role. Pair production follows the same description as that found in the discussion of high-energy electrons (Sec. 3.2). The only difference is that the chain begins with a photon rather than an electron.

In addition, there are second-order effects, such as *Rayleigh scattering*, where the photon wavelength is large enough that it coherently scatters off the entire atom, and photonuclear interactions at higher energies that break up the nucleus [34].

### 3.5 Neutrons

Similar to photons, neutrons are not electrically charged, and thus, they do not undergo Coulomb interactions with electrons and nuclei. Instead, they interact through the strong force with nuclei. Due to the short-range nature of the strong force, these interactions are comparatively rare, as the neutron needs to approach the nucleus closely to interact. Several possible interactions are [8]:

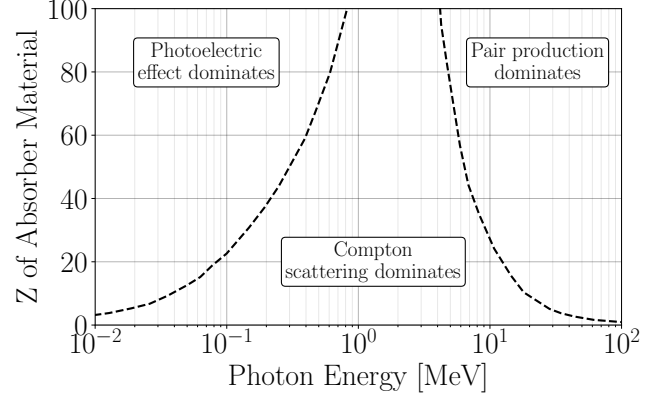


Figure 3.4: Dominant region for the three gamma ray interactions as a function of the photon energy and the target charge number  $Z$ . Modified from Ref. [9]

1. Elastic scattering off a nucleus
2. Inelastic scattering off a nucleus, leaving the nucleus in an excited state that may decay by emitting a gamma ray. To excite the nucleus, the neutron must transfer MeV-scale energies.
3. Neutron capture. At low energies, the neutron might be captured by the nucleus, emitting a gamma ray.
4. Fission
5. Hadronic shower, particularly at high energies ( $> 100$  MeV).

High-energy neutrons produced in the primary cosmic-ray interaction will often collide with another nucleus, creating a similar interaction as the primary cosmic-ray.

# Chapter 4

## DETECTION METHODS

### 4.1 Single Photon Detection: Photomultipliers

Photomultipliers stand as one of the prevalent tools in the toolkit of particle physicists. These devices possess the capability to generate a measurable electrical signal triggered by the interaction of a single photon. The detection of photons allows us to extract information about incident particles by observing the photon emission as the particle loses energy within a material.

A widely utilized instrument for single photon sensing is the photomultiplier tube (PMT), known for its expansive photosensitive coverage at a reasonable cost. Despite its effectiveness, PMTs come with the downside of being bulky, fragile, and requiring high voltage. Other technologies, such as Avalanche Photodiodes (APD) and P-type and N-type semiconductor photodiodes (PIN photodiode), present their own set of advantages and limitations.

Recent advancements in silicon chip manufacturing have given rise to a new breed of photon detectors known as *silicon photomultipliers*, or SiPMs (also abbreviated as SPM). SiPMs bring several advantages over PMTs, including the ability to operate at low voltages (we'll use +28.6V), insensitivity to magnetic fields, robustness, and a compact form factor. Serving as single photon detectors, SiPMs exhibit peak responsivity near the emission peak of typical scintillating materials (420 nm). This modern technology is the foundation of the Desktop Muon Detectors.

SiPMs are composed of densely arranged *microcells* (see Fig. 4.1), where each microcell constitutes a distinct P-type and N-type semiconductor junction (P-N junction). During the formation of a P-N junction, free electrons from the N-type semiconductor diffuse towards the P-type semiconductor, and vice versa, leading to their annihilation. This process establishes an insulating region known as the *depletion region* at the boundary between the P and N-type semiconductors.

As a photon travels through the depletion region and imparts sufficient energy to a bound electron, the electron can transition to the conduction band, generating an electron-hole pair. Applying a potential difference across the P-N junction enables the energized electron to collide with other electrons, initiating their transport into the conduction band. If the potential difference exceeds a critical value ( $> 5 \times 10^5$  V/cm), an electron avalanche or cascade (resembling a Geiger discharge) occurs, wherein a single electron gives rise to a current comprising millions of electrons. Once the flow of electrons begins, the silicon becomes conductive, and a quenching resistor reduces the potential difference across the P-N junction sufficiently to halt the electron cascade. Consequently, each microcell functions as a photon-triggered switch, allowing a brief flow of a small current if struck by a photon. The cumulative current flow is proportional to the number of triggered microcells and, hence, is proportionate to the incident photon flux (when the number of triggering photons far exceeds the number of microcells).

The Desktop Muon Detector utilizes a single On Semiconductor MicroFJ 60035 C-Series SiPM, measuring 7 mm by 7 mm [38] (6 mm by 6 mm sensitive area). These SiPMs are most sensitive in the 420 nm range [39], corresponding to deep blue to purple light. It's worth noting that if the wavelength of a photon exceeds 1000 nm, the absorption length in silicon becomes too large, leading to the SiPM's size becoming impractical. On the other hand, if the photon wavelength is too short, it won't penetrate into the sensitive region of the SiPM, essential for effective detection.

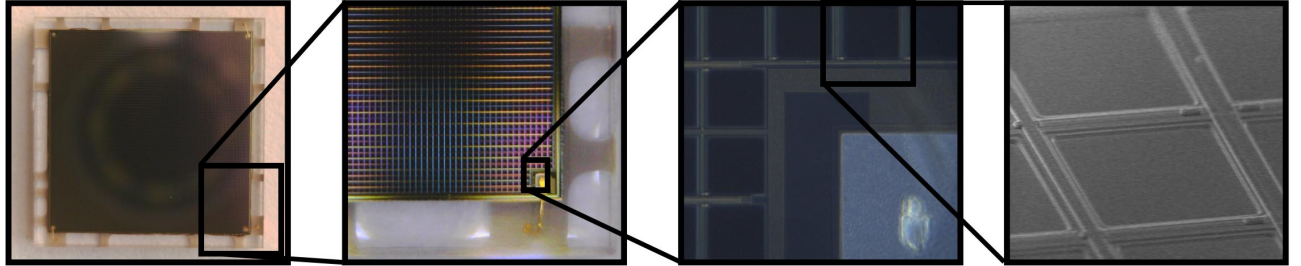


Figure 4.1: An image of a On Semiconductor MicroFJ 60035 J-Series SiPM [38]. Data sheets found in the datasheet folder. The SiPM has a length and width of  $7.00 \pm 0.05$  mm and a thickness of  $0.65 \pm 0.05$  mm. Each one of the tiled squares represents a single microcell, each of which operate independently in Geiger mode.

The applied potential difference is referred to as the "bias voltage," and it determines both the size of the region capable of producing the avalanche (the depletion region) and the energy gained by the electron-hole pair. The "breakdown voltage" signifies the voltage at which the voltage gradient in the depletion region is sufficiently large to initiate a Geiger discharge. For the J-series SiPMs, this typically falls between 24.2 and 24.7 V. If the bias voltage surpasses the breakdown voltage, the microcells will still operate in Geiger mode; however, the electron cascade in the P-N junction will carry more energy, resulting in a linear increase in the charge output (or gain). The disparity between the bias voltage and the breakdown voltage is termed *over-voltage*. It is recommended to maintain an over-voltage between 1.0 and 5.0 V. The Desktop Muon Detectors operate with an over-voltage of 4.0 V, corresponding to a gain of approximately

$4 \times 10^6$  [38].

Thermal fluctuations have the capability to generate electron-hole pairs, mimicking single photon events. For our SiPMs, this phenomenon occurs at a rate of approximately 100 kHz per mm<sup>2</sup>, or several MHz for the entire SiPM. This can pose challenges for applications relying on the distinction between small numbers of photons. It's noteworthy that the breakdown voltage needed to initiate the electron cascade is temperature-dependent; lower temperatures correspond to lower breakdown voltages. For every 8°C decrease in temperature, the dark rate decreases by a factor of two.

## 4.2 Scintillators

Scintillators are materials designed to absorb energy through Coulomb interactions and subsequently re-emit that energy in the form of electromagnetic radiation, known as scintillation light. Scintillators can take various forms; for instance, they may be grown as crystals (referred to as inorganic scintillators) with added dopants, or they might consist of a fluorescing material embedded in plastic materials such as polystyrene or acrylic, or mixed into liquids like toluene or mineral oil—examples of organic scintillators.

Inorganic scintillators are typically more expensive, but they often have higher density and emit more photons per unit energy deposited. This characteristic makes them particularly useful for calorimetry. On the other hand, organic scintillators are generally more affordable since the fluorescent material is suspended in a common, often low-density material like plastic, facilitating ease of manufacturing.

Scintillators are highly valuable materials as they emit light in proportion to the energy deposited in the material. Consequently, a common metric used to assess the quality of a scintillator is expressed as the number of photons emitted per absorbed MeV of energy, often referred to as the scintillator efficiency. For instance, a typical organic scintillator may exhibit an efficiency of 10,000 photons/MeV. Another crucial parameter associated with scintillators is the photon emission profile, determining the wavelengths of emitted photons after de-excitation. Moreover, scintillators must be transparent to scintillation light to enable its propagation to the photon detector. Plastic scintillators may have attenuation lengths ranging from 0.3 meters to 3 meters [40, 41], while liquid scintillators like Linear Alkyl Benzene (LAB) can have attenuation lengths of up to 25 meters [42]. Scintillators also exhibit a very fast response and recovery, with excitation and de-excitation of the fluorescing molecules occurring on the order of nanoseconds for organic scintillators and hundreds of nanoseconds for inorganic scintillators.

The CosmicWatch Desktop Muon Detector was designed using an organic plastic scintillator, comprising a polystyrene base (essentially an inexpensive transparent plastic) mixed with a primary dopant of 1% by weight of POP (2,5-diphenyloxazole) and 0.03% secondary dopant

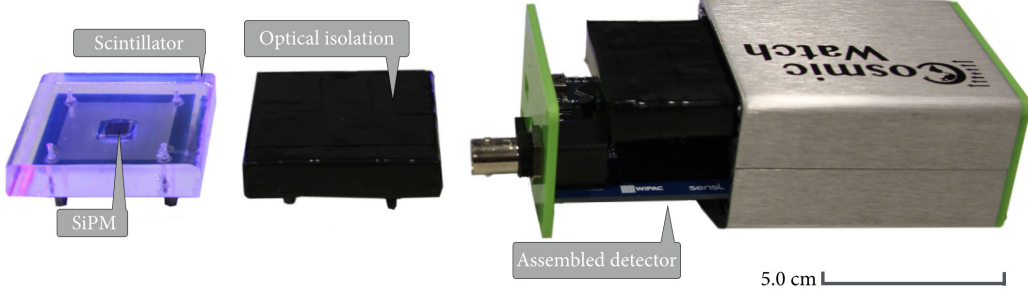


Figure 4.3: The components of the Desktop Muon Detector. Modified from Ref. [47].

POPOP (1,4-bis[2-(5-phenyloxazolyl)]benzene) [43]<sup>1</sup>. This plastic scintillator does not emit light below 400 nm and has a maximum emission around 420 nm (deep-purple light). Developed by FermiLab for the MiNOS [45]/MINER $\nu$ A [46] experiments, we will focus on a description of organic scintillators below. However, a comprehensive description of inorganic scintillators can be found in Ref. [44].

The plastic scintillator consists of three essential components:

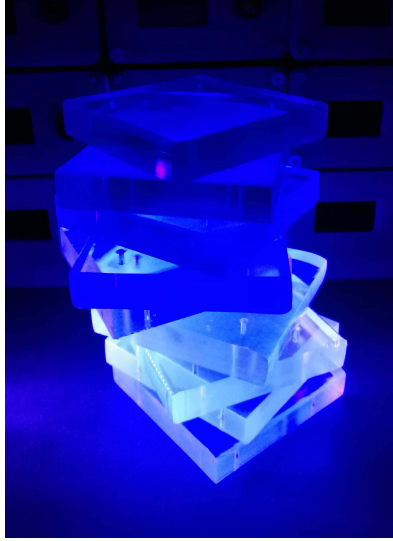


Figure 4.2: A UV flash light illuminating scintillator.

- A transparent base, visible in the visible spectrum, used to suspend the fluorescent material. This can be a type of plastic (such as polystyrene) or a transparent liquid like mineral oil.
- A primary fluorescing agent excited by the energy transfer from the incident charged particle. The de-excitation of the primary fluorescent material releases ultraviolet (UV) light. UV light has a limited travel distance in the base (on the order of millimeters) before being absorbed.
- A secondary fluorescent agent that absorbs the UV light and converts it to the visible spectrum. The visible light then travels through the scintillator, internally reflecting off the walls until it is absorbed. Ideally, some of the visible light will strike the photon sensor coupled to the scintillator.

A straightforward representation of the UV conversion process is depicted in Fig. 4.2. In this illustration, several pieces of scintillator are illuminated with a UV flashlight. The UV light is absorbed by the secondary fluorescent agent and re-emitted as deep blue/purple light. A polystyrene-

---

<sup>1</sup>Interestingly, PPO was one of the earliest compounds investigated as a scintillator solute by Hayes et al. (see Ref. [44]) from 1953-1958 and is still widely used

based scintillator typically has a density of approximately  $1.032 \text{ g/cm}^3$  (similar to water) and a refractive index at standard atmospheric pressure of  $n = 1.581$  [9].

The Desktop Muon Detector couples a SiPM (see Sec. 4.1) to a slab of scintillator through optical gel, which reduces the probability of a photon being reflected at the interface by matching the refractive index from the scintillator to the housing of the SiPM, eliminating the air gap with  $n = 1.0$ . Additionally, the remaining surface is wrapped in aluminum foil to reflect photons that escape the scintillator. The entire assembly is then covered with 2-3 layers of black electrical tape to ensure light-tightness. The assembly of the detector is illustrated in Fig. 4.3.

# Chapter 5

## THE COSMICWATCH DETECTOR

### 5.1 Introduction to the Detector

As detailed in Ref. [47], the CosmicWatch Desktop Muon Detector comprises a  $5 \times 5 \times 1$  cm<sup>3</sup> slab of plastic scintillator equipped with a silicon photomultiplier (SiPM). When a charged particle traverses the scintillator and deposits energy, a portion of that energy is re-emitted isotropically along the particle track in the form of photons. Photons reaching the photosensitive area of the SiPM can induce a Geiger discharge in the SiPM microcells. The microcells, when discharged, generate a measurable current. A single photon can trigger a single microcell (ignoring second-order effects), while multiple photons may trigger multiple cells. The resulting current is directed through a custom-designed printed circuit board (PCB), which amplifies and shapes the signal to make it suitable for measurement by an inexpensive microcontroller (in this case, the Raspberry Pi Pico). The RP Pico records the event timestamp and peak value on the analog-to-digital converter (ADC). The measured peak ADC value is then converted back into a SiPM peak voltage, which is proportional to the number of photons incident on the SiPM. If the measured ADC value exceeds a software-defined threshold, the microcontroller logs the event data either onto a microSD card or directly to a computer via a USB connection. For each event, the detector logs the event number, event time relative to the detector start time, measured 12-bit ADC value at two levels of pulse amplification (HGain and LGain), calculated SiPM peak voltage (proportional to the SiPM pulse charge), event dead-time, temperature, pressure, and whether a coincident detector also registered a pulse.

When the detector is directly connected to a computer via a USB cable, data can be recorded through a Python-based program that adds a local timestamp from the computer. The RP Pico clock drifts over time (seconds per day), so it's often desired to have a more accurate and precise timestamp. If your computer is set to "Set date & time automatically" it uses the Network Time Protocol (NTP), which should keep the precision and accuracy of the timestamp to within roughly 5ms.

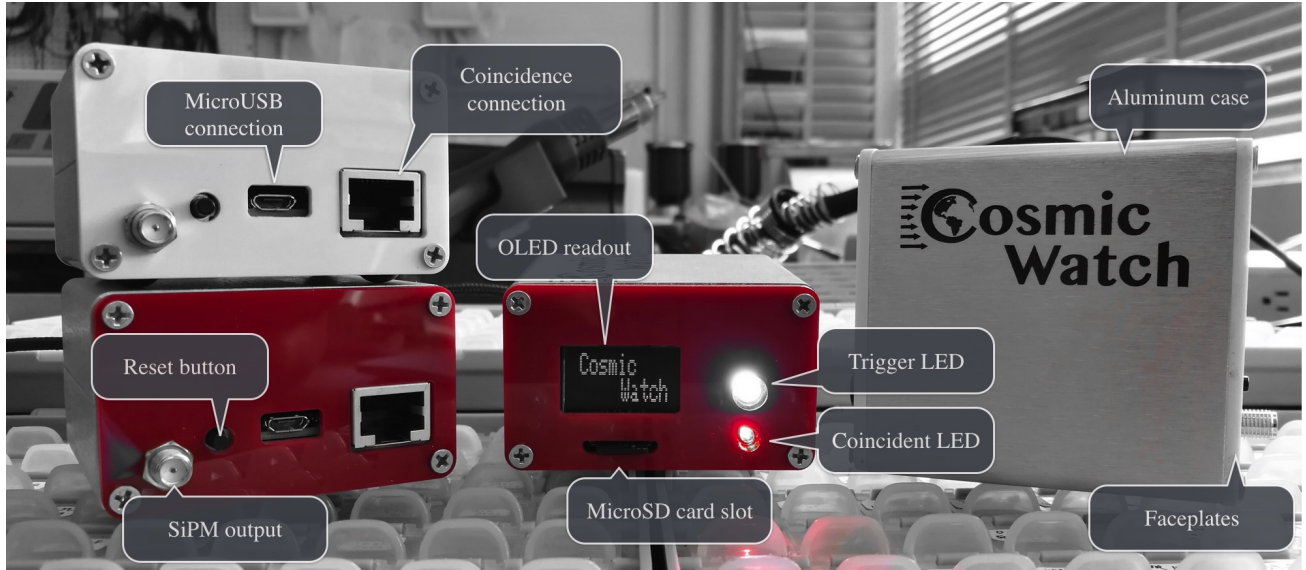


Figure 5.1: An array of Desktop Muon Detectors.

An array of complete detectors is depicted in Fig. 5.1. The front of the detector is equipped with a reset button, two LEDs, and a built-in 0.96" OLED screen displaying information such as the count number since the last reset, total uptime, count rate (compensated for detector dead-time), and an indication bar proportional to the calculated SiPM peak voltage of the last triggered event. Multiple detectors can be interconnected using a common Ethernet cable to perform a *coincidence measurement* (refer to Sec. ??). The top 5 mm LED triggers on all events, while the bottom 3 mm LED triggers only on coincident events.

The detector was measured to consume 0.4 W and can be powered through any USB connection supplying more than 4.5 V. This includes the USB port on a computer, USB power bank, or power outlet USB. The total mass of the detector, including the aluminum case, is 200 g, and the outer dimensions are 66.4 mm × 70.0 mm × 39.9 mm. Excluding the aluminum enclosure and end-plates, the detector has a mass of 100 g.

The backside of the detector features a micro USB port for powering the detector, uploading new code to the RP Pico, or directly recording data through a USB port. It also includes an Ethernet connection for linking multiple detectors to perform coincidence measurements, a microSD card that logs data when inserted, and an BNC connection directly connected to the SiPM output.

## 5.2 Recording data

Data can be collected from the Desktop Muon Detector in many ways:

1. **(Recommended) Through a microSD card:** Each time the detector is reset or powered on, a new file is created with a filename that counts sequentially upwards from the previous file. An "M" or "C" indicates whether the detector was in *master mode*, indicating that a coincidence detector was not used during startup, or *coincident mode*, indicating that a second detector was observed. Extracting data using the microSD card is least prone to error and likely the simplest.
2. **Directly to a computer through a microUSB cable:** When the detector is plugged into a computer USB port, and the import\_data.py is run using Python 3 (with appropriate libraries installed), the user is prompted to supply the path and name of the file to where the data is to be stored. It will then begin recording the data in real-time to the output file.
3. **In real-time via a serial monitor:** When a detector is plugged into the computer, the detector sends the triggered data through the serial connection (USB micro cable). If you have a serial monitor, you can read the data. We communicate at baud rate is 115200 bits per second. The simplest serial monitor is the Arduino IDE. The data can be seen accumulating in real-time in the serial monitor (top right magnifying glass). The data can be copied and pasted into a text editor for later analysis.
4. **Simply through the OLED screen:** The OLED readout accounts for the detector dead time. Therefore, if you simply need to know the count rate, the OLED readout might be enough for your measurement. That being said, the data is still recorded to the microSD card.

The data is always saved in a simple to use .TXT file. Comments are always indicated with the "#" marker. Each row is a different event, and each column represents some different property of the measurement. The columns are tab-delimited. The detector actually starts out printing a set of diagnostics, which shouldn't be particularly relevant to this document. An example of the data is shown in Fig. 5.2.

The data shown in Fig. 5.2 is formatted into tab-delimited columns, each of which is labeled in the header and defined as follows:

- **Event:** The event number of the detector.
- **TimeStamp [ms]:** The total elapsed time, measured in milliseconds. This is only accurate to roughly  $\pm 1$  min per day and precise to the nearest millisecond.
- **ADC1 [0-4095]:** The high gain ADC measurement for the event. The RP Pico has a 12-bit ADC, meaning the values reported are from 0-4095 ( $2^{12}$  values). The ADC is referenced between ground and 3.3 V.
- **ADC2 [0-4095]:** The low gain ADC measurement for the event. The RP Pico has a 12-bit ADC, meaning the values reported are from 0-4095 ( $2^{12}$  values).

```
#####
### CosmicWatch: The Desktop Muon Detector
### Device ID: Tweety
### Launch time: 16:22:11 21/8/2020
### Questions? Email Spencer N. Axani (saxani@mit.edu)
### Event Time Date TimeStamp[ms] ADC1 ADC2 SiPM[mV] Temp[C] Pressure[Pa] DeadTime[us] Coincident
#####
1    17:22:11    21/8/2020     697   222.27  5.99   7.92   0.00   0.00   5519   0
2    17:22:11    21/8/2020     753   131.77  5.64   5.69   0.00   0.00   4804   1
3    17:22:11    21/8/2020     978   486.97  60.39  13.94   0.00   0.00   776    0
4    17:22:12    21/8/2020    1563   717.02  262.26  23.18   0.00   0.00   6310   0
5    17:22:12    21/8/2020    1590   347.42  7.59   10.23   0.00   0.00   778    0
6    17:22:12    21/8/2020    1804   462.43  53.72  13.19   0.00   0.00   771    1
7    17:22:13    21/8/2020    2226   392.39  12.25  11.26   0.00   0.00   6311   0
8    17:22:13    21/8/2020    2260   488.40  51.75  13.99   0.00   0.00   778    0
9    17:22:13    21/8/2020    2636   219.94  5.78   7.87   0.00   0.00   776    0
```

Figure 5.2: Example data format. The header for the file is commented out with "#" and then there are nine events that follow. This data was recorded using the detector named "Tweety." The definitions of the columns are listed in the header, as well as a more descriptive description in the text below.

- **SiPM [mV]:** The calculated SiPM peak voltage. This is a number calculated from the measured ADC value. Small SiPM pulses are primarily measured using the high-gain ADC channel (HGain), while large SiPM pulses primarily use the low-gain channel (LGain). It represents a number roughly proportional to the number of photons that triggered the SiPM.
- **Temp [°C]:** The measured temperature of the detector via the on-board BMP280 temperature sensor. Measured in degrees Celsius.
- **Pressure [Pa]:** The measured pressure of the detector via the on-board BMP280 pressure sensor. Measured in degrees Pascals.
- **Dead-time [μs]:** The dead-time since the previous event in microseconds. This must be accounted for when making any rate measurement. Take the total time and subtract the total deadtime to get livetime.
- **Coincident:** If the detector observes a coincidence signal in the RJ45 connection (Ethernet connection) within approximately 3 us, the event is considered coincident, and this value is set to "1"; otherwise, it's "0." Events with a "1" in this column are overwhelmingly due to cosmic ray muon interactions.

### 5.3 Setting detectors in master and coincidence mode

Many measurements in this document rely on the detectors operating in *coincidence mode* (e.g., see Sec. ??). This mode allows us to improve the purity of the cosmic ray muon sample by rejecting events that likely came from interactions with radioactive backgrounds. Coincidence mode requires two detectors connected together using an Ethernet cable (referred to as the



Figure 5.4: Two detectors in coincidence mode, powered by a USB power bank. Every time a detector triggers on an event, it sends a digital pulse to the other detector. If the other detector also triggers on a pulse during at the same time, the event is said to be coincident and is very likely to have been caused by a cosmic ray muon. Coincident events flash the coincidence LED (red LED on the front plate).

*coincidence cable*). Once connected, only one of the detectors requires power, while the others are powered through one of the internal wires in the cable.

To set the detectors into the coincident configuration, simply reset both detectors simultaneously while they are connected together. Alternatively, you can unplug the power cable (microUSB) and plug it back in. The detectors will acknowledge the presence of a coincidence detector by brightly illuminating both LEDs on the front panel for 1 second. An example of two detectors being set up in coincidence mode is shown in Fig. 5.4.

All events are always recorded using the default settings in the software. However, coincident events will be designated in the data with a "1" in the coincident column. In Coincidence mode, the OLED screen will display both the full trigger rate and the coincidence rate.

Coincident events are likely to be due to a cosmic-ray muon, as backgrounds and accidental coincidences are unlikely to trigger both detectors simultaneously. A summary of why the purity of the cosmic-ray muon signal increases in coincidence mode is provided below.

Master mode	Coincidence mode
Total counts: 12588	Total counts: 12588
Uptime: 1:10:11	Uptime: 1:10:11
M --	Rate: 3.140 +/- 0.21 Hz
Rate: 3.140 +/- 0.21 Hz	Rate: 0.170 +/- 0.01 Hz

Figure 5.3: The OLED output when set in Master (left) and Coincidence (right) mode. In Master mode, the third line displays an "M" and a bar indicating the pulse amplitude of the last event. In Coincidence mode, both the full trigger rate and coincidence rate are readout in the third and fourth line.

- Alpha particles will not penetrate a single detector (either the aluminum enclosure or even the black electrical tape) and therefore cannot trigger both the master and coincident detector at the same time.
- Beta particles can be significantly attenuated by the aluminum case, and have a significant chance of scattering, thus losing energy. It's unlikely that the beta particle will be able to deposit sufficient energy within the scintillator of the master, exit, then depositing sufficient energy in the coincidence detector.
- Gamma rays can penetrate the aluminum enclosure and plastic scintillator, however they have a significant chance of Compton scattering, which will change the direction. If a gamma ray does interact with both detectors, this means that it likely Compton scattered off the scintillator slabs, lost sufficient energy to trigger the detector, then Compton scattered or photoelectrically absorbed in the second detector, also depositing sufficient energy to trigger the detector. This process will be rare, and represents a small part of the coincidence signal (an estimate of this rate is found in Sec. 9.5).
- Accidental coincidences from uncorrelated random events overlapping in the coincident trigger window is also a rather rare occurrence at the standard background rates. This will be elaborated on in Sec. 7.
- A typical minimum ionizing muon passing through the slab of scintillator will typically deposit more than 2-3 MeV of energy in the scintillator, without being deflected. If the muon passes through both scintillators, it will likely trigger both detectors simultaneously.

## 5.4 What Can Possibly Go Wrong?

When conducting measurements with the Desktop Muon Detectors, it is essential to consider a few key factors.

1. The RP Pico is an inexpensive (4 USD) and relatively slow device compared to other much more expensive devices. While it is faster than some microcontrollers, inherent issues arise due to its speed limitations. A crucial aspect of any rate measurement with the Desktop Muon Detector is that every command, whether it involves simple arithmetic or printing detector information to the serial port or microSD card, takes time to execute. Accounting for the time each command takes is important because the detector cannot trigger an event while it is busy. The term associated with the time during which the detector is unable to make a measurement is referred to as *dead-time*. The detector software code calculates the dead-time by measuring the time each command takes in microseconds. The dead-time between each event is recorded in the output file. To obtain an accurate measurement of the time the detector was able to make a measurement, the dead-time must be subtracted from the up-time; the result is termed *live-time*. Dead-time is a common feature in all particle physics detectors, but it is particularly crucial for us due to the limited speed of the RP Pico and its dual-core processor.

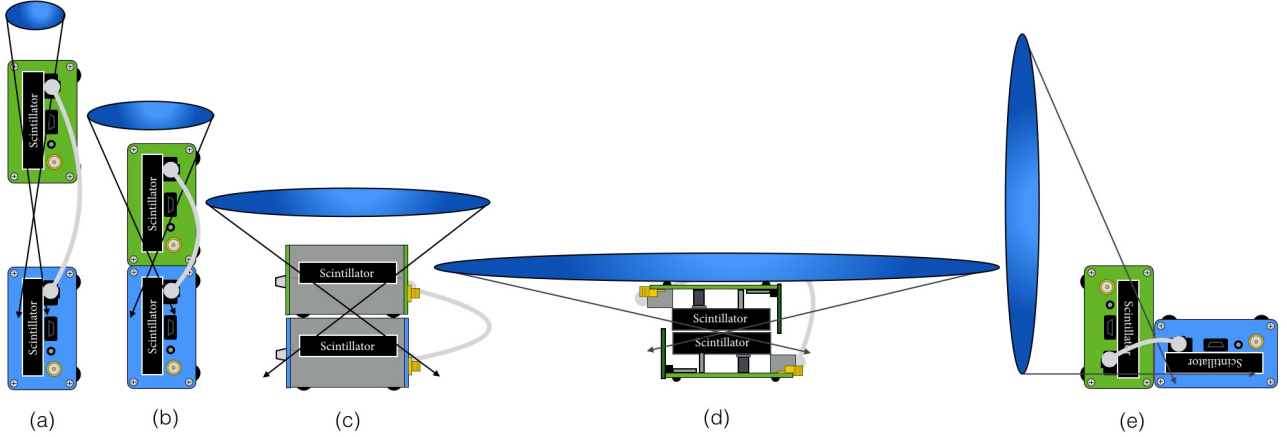


Figure 5.6: This figure shows several configurations for setting up the detectors in coincidence mode. Moving from left to right the solid angle subtended between detectors increases (illustrated as the blue ovals above the detectors) as well as the coincidence rate as measured by the coincident detector.

2. The orientation of the master and coincident detectors during a measurement will yield different characteristics. When conducting a coincidence measurement, careful consideration of what is being measured and how the orientation impacts the measurement is crucial. For instance, when interested in the angular spectrum of cosmic-ray muons, the goal is to selectively accept muons originating from a small solid angle (a specific area of the sky). Figure 5.6 illustrates several possible configurations. On the left side of Figure 5.6, labeled as (a), two detectors spaced a few centimeters apart are connected with a coincidence cable. In this setup, only muons traveling downward through the blue area can trigger both detectors (consider the trajectories that can trigger both detectors). This configuration is suitable for measuring the angular distribution of cosmic-ray muons. Figure 5.6 (d) depicts a configuration where both detectors will trigger from down-going muons over a much larger solid angle. This (or (c)) configuration is commonly employed to extract strictly muon rate information, as it provides the highest statistics by examining a larger solid angle.

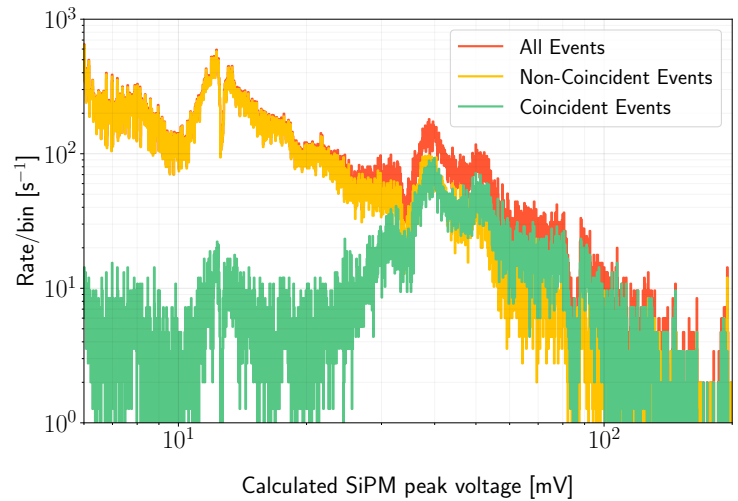


Figure 5.5: A coincidence measurement showing the calculated SiPM pulse amplitude for the coincident events and non-coincident events.

32

3. Two distinct events might accidentally trigger both the master and coincident detectors if they happen to occur within the coincidence time window. This probability increases at higher count rates. Assuming that individual count rates follow Poisson statistics and that the two detectors are independent, the probability of observing  $n$  events when the mean number of events is expected to be  $\mu$  is described by the Poisson distribution:

$$f(n, \mu) = \frac{\mu^n e^{-\mu}}{n!} \quad (5.1)$$

Following Ref. [9], let the count rates on the two detectors be  $N_1$  and  $N_2$ , and the coincidence window (the time window in which an event will be labeled as a coincident event) be  $\tau$ . The average count rate for both detectors at sea level is approximately 3 Hz, and given a coincident time window of roughly  $3\mu\text{s}$ , we expect, on average, 0.000009 events in the time window ( $N_{1,2} \times \tau$ ). Therefore, the probability of observing zero events in the time window is  $f(0, 9 \times 10^{-6})$ , and the probability of one detector observing an event in the coincident time window is  $1 - f(0, 9 \times 10^{-6})$ . Since the second detector could have also triggered first, the rate of accidental triggers is given by:  $R = 2N_1 N_2 \tau$ . This corresponds to an accidental coincident rate for two detectors of 1 every 55,000 events, or roughly five events per day using two detectors, at sea level.

# Chapter 6

## HOW TO BUILD A COSMICWATCH DETECTOR

### 6.1 Overview

You will be given all the components to build the detectors. Your goal is to put the components in the correct place and make sure they are securely attached.

The construction of the detector will be divided into four parts. (1) First, we will populate the printed circuit boards (PCB). (2) Then, we will interface the SiPM with the scintillator. (3) We will test the detectors to make sure everything is working (troubleshooting section). (4) The final section is devoted to uploading the code to the Raspberry Pi Pico microcontroller.

#### 6.1.1 Populating the PCB

Here is a step-by-step description of how to populate the PCBs. The components are almost all surface mount technology (SMT), which means that they are small and sit on top of the board rather than with legs passing through it (through-hole components). We will be using 0805 SMT components. This represents the size, where the majority of the components are 0.08 inches by 0.05 inches. The first time you use them, they may look small, but you'll get used to them with a bit of practice. A pro may commonly use 0402 components, more than a forth the size. The 0805 SMT components are a good size to learn about soldering. All the components we'll need are listed on the PCB Reference sheet, located in the GitHub PCB directory. The reference sheet includes the identifier and the value of the component. We use the identifier R to represent resistors, C for capacitors, L for inductors, U for integrated circuits, and D for Diodes. Also note that the larger components, like the RP Pico, is drawn on the Silk screen of the PCB in order to help you orientate the part. Make sure you put each component on the

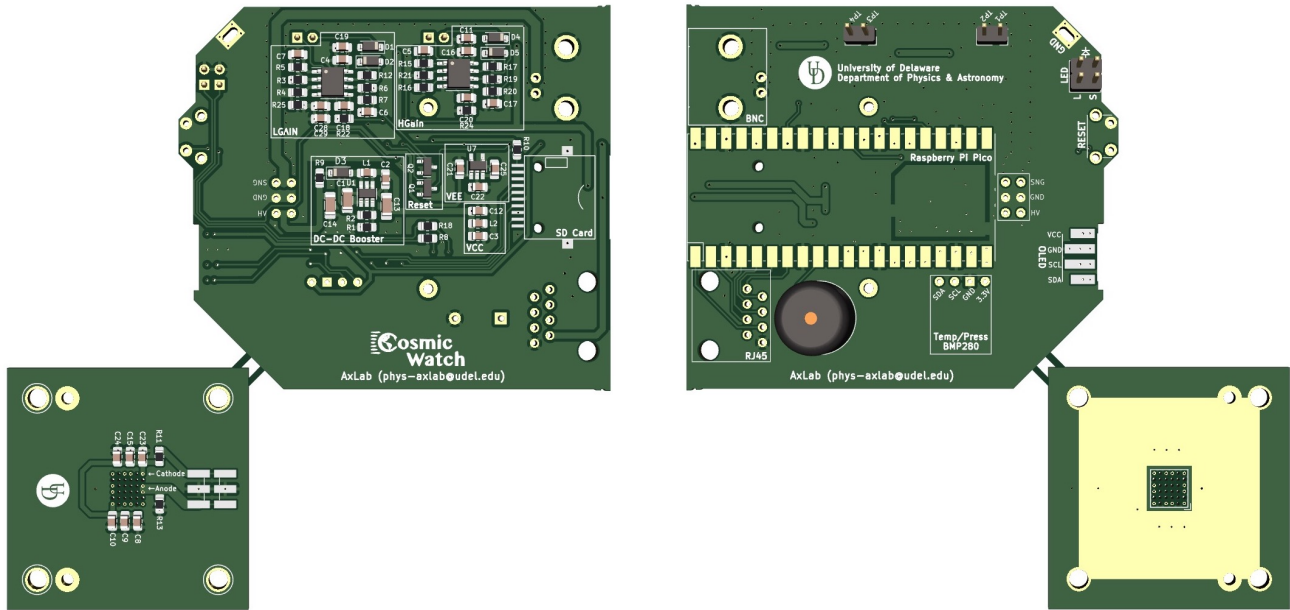


Figure 6.1: A 3D rendering of the printed circuit boards. Right: Top view. Left: Bottom.

side of the board with it's silk screen markings. A rendering of the PCB is shown in Fig. 6.1.

## Soldering SMT components

Soldering involves melting a lead-based piece of metal (solder) to form the connection between the component and the PCB. There exists non-lead based solders, but I've only found them to be terrible. You will use a hot soldering iron, maybe set to around 750°F. This isn't hot enough to damage the PCBs or components (except the plastic ones). You will hold the soldering iron with your dominant hand, and the solder with your sub-dominant hand. We call the components position on the board the "footprint," and each metal part of the footprint a "pad."

**Tip:** It's best to orientate the part rather than awkwardly orientate your hands while soldering. Move the PCB into a comfortable position for each solder joint.

Soldering a component in place always involves the same procedure for all components. Practice this routine with each component. The philosophy is to get one pad connected to the component, inspect the orientation, then continue with the other pad(s) and go back to the original one to clean it up. That is, the first solder joint is just to hold it in place. It's easy to move a piece that only has one soldered joint, and very difficult if you have multiple pads constraining the component. Here's the procedure:

1. Determine the component you are mounting on the board from the Reference List. Find that component on the board.
2. Add solder to just one of the footprints pad.
3. Pick the component up with tweezers, bring it close to the footprint. Make sure that the component is flat against the PCB.
4. Melt the solder on the pad from Step 2. And bring your component into place. Keep holding it with the tweezers.
5. If you are happy with the component position, remove the heat, and let the solder solidify, then let go with the tweezers.
6. Inspect. Is it flat against the board? Is it in the correct orientation?
7. Finalize. If it looks good, solder the other connections.
8. Perfect. Now that the component is secured to the board, you can go back and add new solder to the joint to ensure a good connection.

Follow and master the above. Start with the first component on the reference list. We've made this list such a way that that the first components are good to learn on. By the end, you should be able to add a single component in seconds.

NOTE: some components have a direction. We've noted it on the reference list. Diodes have directions. One of the capacitors has a direction. The ICs have direction.

The hardest component is the SiPM. We'll do this last. Make sure you have the SiPM correctly orientated. Also, make sure you can measure a voltage drop across the Cathode and Anode of the SiPM PCB (annotated on the back of the PCB) of roughly 0.5V. This can be done using the diode function on the multimeter, with the red terminal on the Anode and the black terminal on the Cathode. If you don't see any voltage drop, it means your SiPM isn't connected. You'll need to try to remount it.

The PCB reference list also includes checkpoints, in which you can test various parts of the circuit. For example, after populating the components to generate the -5V rail, you plug the board in and test it to make sure it's working properly. If anything doesn't seem to be working, the most common problem is not having a good solder connection. You can add new solder to the relavent components to fix this issue. The second most common problem will likely be an incorrect part. If you suspect this, we can always double check with you.

You can see a completed board below.

## Interfacing the SiPM to the scintillator

Once you have all the components populated, including the SiPM, it's time to interface the SiPM to the scintillator. Make sure you have the aluminum standoffs on the SiPM PCB, securely fastened (past hand tight) with the size 0 screw.

First, wrap the scintillator in a single layer of aluminum foil, leaving a roughly  $2 \times 2 \text{ cm}^2$  open area for the SiPM face. Add a small amount of black electrical tape to hold it in place, as shown in the Fig. ???. It's hard to see the four mounting holes with when the scintillator is wrapped in aluminum foil; you can simply apply some pressure to the location of the holes to have their outline pop through the foil/tape. I would use the tweezers to poke holes thorough the foil/tape, to help align the SiPM board.

Apply a generous amount of optical gel (silicon-based optical PMT coupling gel) to the surface for the SiPM. Drop in the four #2 screws in to the outermost SiPM PCB holes, and screw the board into the scintillator. Remember that the SiPM is roughly 0.65mm thick, so there should be a gap of roughly that size between the PCB and scintillator.

If all went according to plan (probably 30% chance that you won't run into problems), you should be able to plug your SiPM+ scintillator combo into your Main PCB. When you supply power to the RP Pico, the detector should trigger at roughly 2.5Hz. About 0.4Hz of this are muons; the rest is mainly backgrounds related to environment radioactive decays. If you like, you can insert the detector into the case, add the LED holders to the front face plate, and rubber feet to the bottom of the case. The case is purely cosmetic and protective. If your measurement does not need a case, you can run the detector without it.

You can now plug your detector into another one with the RJ45 cable. When you supply power to one of the detectors, they will both boot up, and if they see each other, they will flash a bright LED light for 1seconds, indicating that they are entering "coincidence mode." In coincidence mode, events that are observed by both detectors (within a few microsecond time window) are tagged as coincident and are very likely caused by a muon. If your detectors on in their cases, sitting one-on-top of the other, you should see something like 0.14Hz of muons. If you want to measure all the muons, remove the detectors from their cases, and place them one-on-top of each other with the scintillator touching. See for example Fig. 5.6. You now have a muon telescope!

## Troubleshooting

If you followed the PCB reference sheet, you would have hit various checks to test different parts of your circuit. For this section, I'll assume you ran into some problem, and describe common troubleshooting techniques.

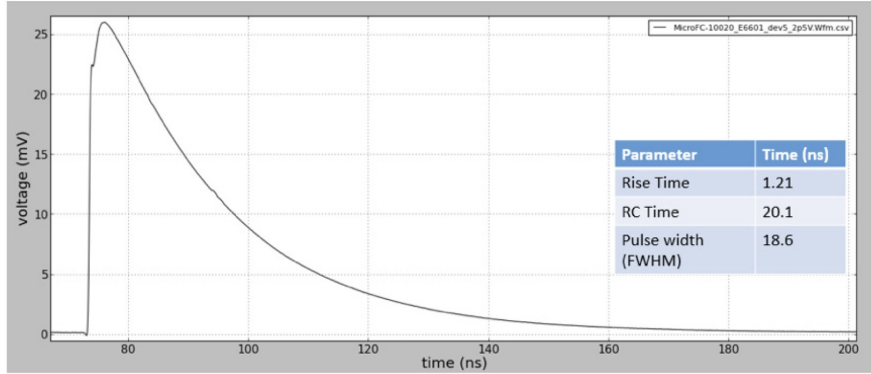


Figure 6.2: A typical SiPM pulse. Given the scale, I estimate this is about 100 photons given a gain of  $4 \times 10^6$ .

- **I see smoke or a high power draw ( $>0.5\text{W}$ ).** You have a short somewhere, a misplaced component, or component with the incorrect orientation. Disconnect immediately and go through your circuit again. The most common mistake is mounting the LT1807 op amp backwards. The pin 1 needs to be on the correct side of the footprint. You can often identify the problematic component by touching various parts of the board. None should be hot. If hot, there's likely a problem in that area.
- **I'm not seeing  $+29.5\text{V}$  between the HV and GND 6-pin connector going to the SiPM.** This will be caused by a problem in the DC-DC booster area of the PCB. First, check the orientation of the MAX5026 DC-DC booster.
- **I have  $29.5\text{V}$  going to the SiPM, but I don't see any  $10\text{mV}$   $100\text{ns}$  pulses out of the BNC connector (example pulse shown in Fig. 6.2).** First make sure that you are correctly setting up the oscilloscope; maybe  $10\text{mV}$  per division and  $100\text{ns}$  per vertical division. Trigger on the correct channel. If you still don't see anything, your problem is with the SiPM PCB. You likely have one of two issues. The smallest light leak will cause problems. Add some additional tape, look for holes in the corners, et cetera. Otherwise, the problem could be with the SiPM, which isn't great, since you have to unwrap the scintillator to check it. The most common problem is that you mounted the SiPM in the incorrect orientation, or a poor connection on the SiPM. Before wrapping up the SiPM scintillator, it's good to check that you have approximately a  $0.5\text{V}$  voltage drop between the Anode and Cathode of the SiPM PCB. This is a good way to test if your SiPM is connected.
- **I see pulses out of the BNC, but my detector isn't triggering.** If this is the case, it means you have a problem with either/or the amplifiers and peak detectors. We can use the testpoints (TP1, TP2, TP3, TP4) to identify the problematic area. First, setup the oscilloscope to trigger on the output of the BNC, then connect the scope probe to channel two and see if you have  $50\times$  amplification on TP1 and  $250\times$  amplification on TP3. If no, that narrows down the problem to the respective amplifiers. If it looks good, check TP4, the high gain peak detector. You should see pulses that are  $250\times$  larger than the output of

the BNC, but they decay over 100s of microseconds. If you see this, your detector should be triggering, if not, make sure you have the correct software. You can also check TP2, the low gain peak detector. This should be 50x larger than the BNC pulse, but also decay over 100s of microseconds.

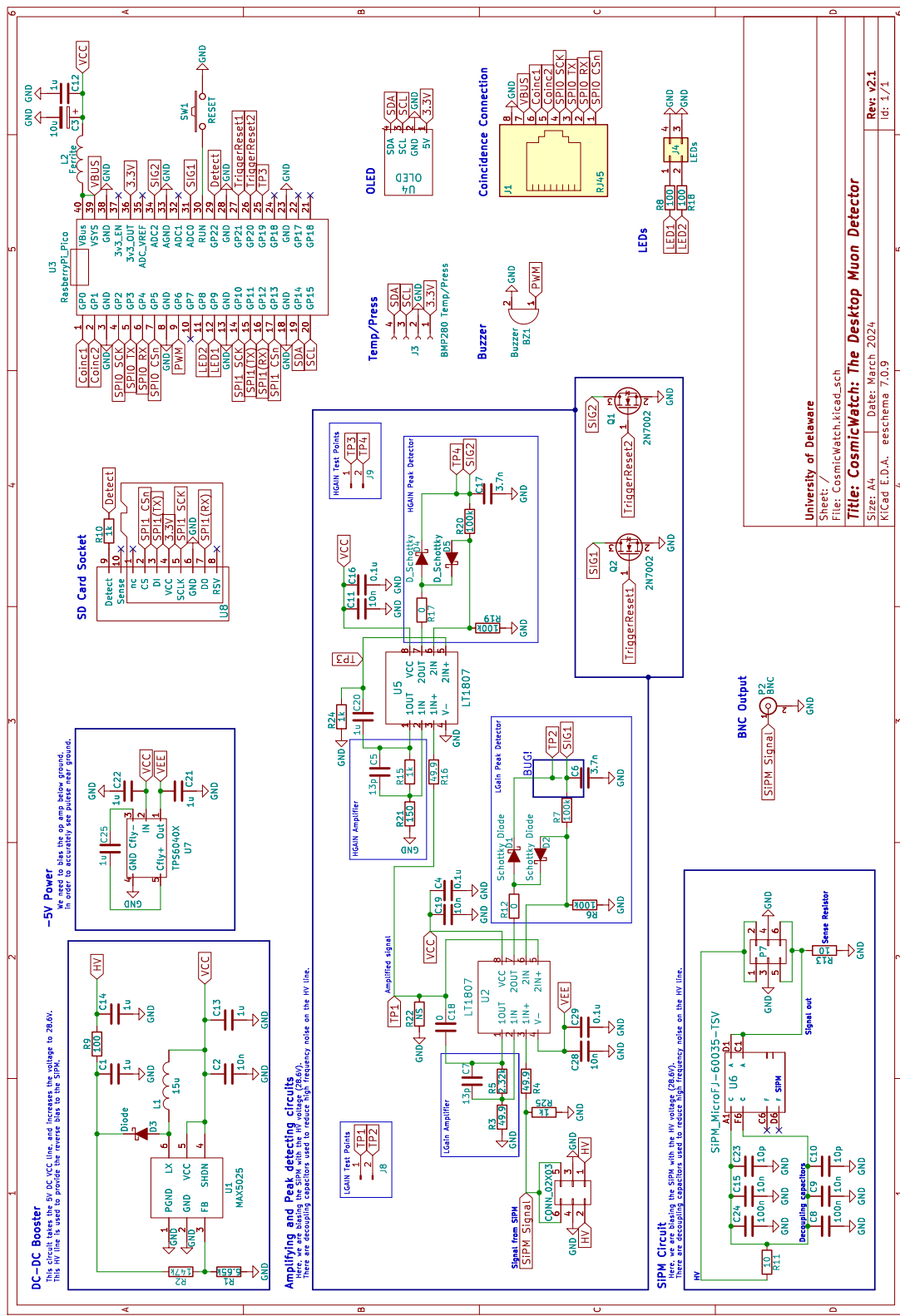


Figure 6.3: The circuit diagram of the UD version. Vector version available on GitHub.

# Chapter 7

## TESTED MEASUREMENTS YOU CAN CHOOSE FROM

You will design your own experiment for this laboratory class. The list below are some measurements that can be done at home, the lab, or office. Feel free to choose from this list or develop your own idea! Inspiration for new ideas may come from measurements described in Sec. 9.

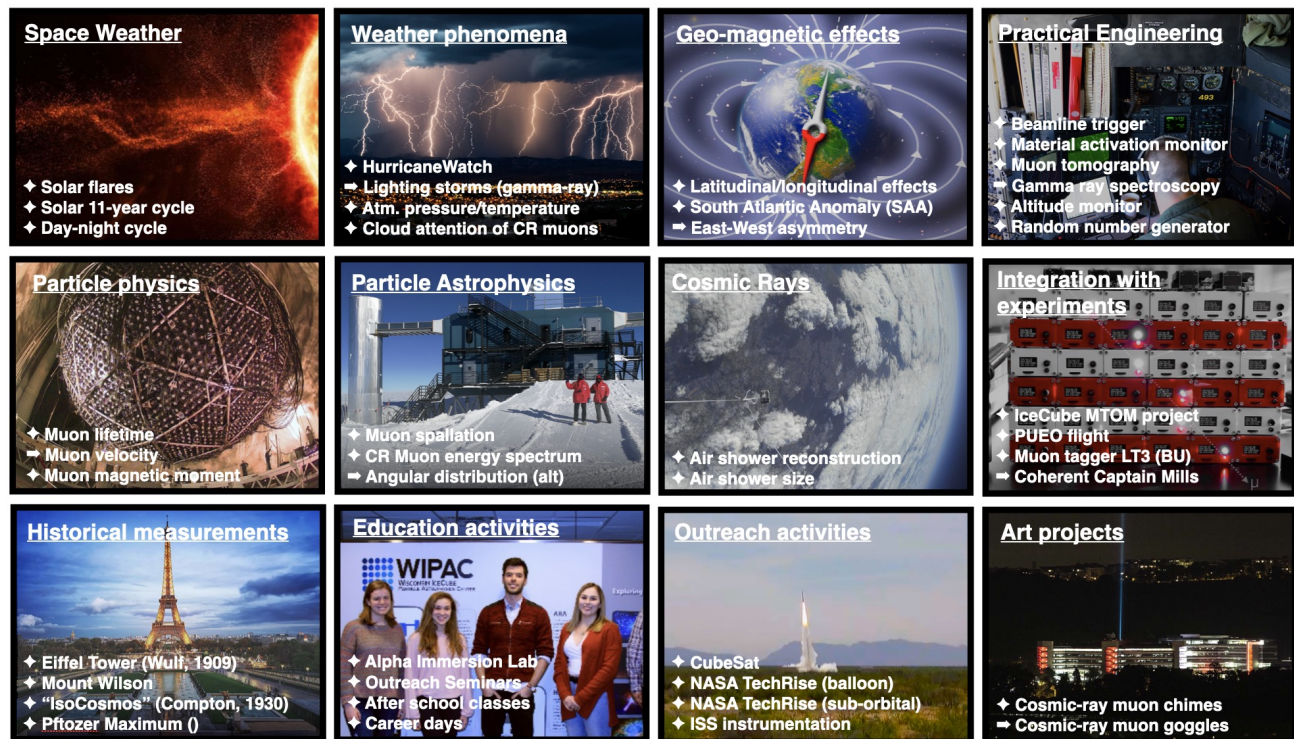


Figure 7.1: This figure gives you an overview of the scope of the muon detectors. Some of these measurements will be described below, other we are still working on.

## 7.1 Cosmic-ray Muon Angular Distribution

This measurement illustrates the cosmic-ray muon angular dependence measured near sea level (it was performed in Madison, WI, at 266 m above sea level) and was previously described in Ref. [47]. Here, two detectors were set to coincidence mode and placed side-by-side as in configuration (a) of Fig. 5.6, spaced 52 mm apart, inside their aluminum enclosures. The distance was chosen such that we gain sufficient statistics throughout a single day. If the detectors are placed too far apart, the count rate drops significantly, and accidental coincidences can dominate the signal.

The angle of the detectors was determined by securing the detectors to a 100 cm long rectangular bar and then positioning the bar against a wall at a known height (see Fig. 7.2 (right)). It is important when making this measurement that the angle of the detectors is accurately measured. Fig. 7.2 (left) shows the measured relative rate as a function of zenith angle (with zero radians representing vertical). Each data point represents approximately 10 hours of data, and the rate uncertainties are statistical. The horizontal (x-axis) uncertainties represent the calculated opening angle of the two detectors when spaced 52 mm apart. The measurement at  $\theta = \pi/2$  is divided by 2, since at this angle it accepts cosmic-ray muons from both directions, whereas all the other angles only accept down-going muons.

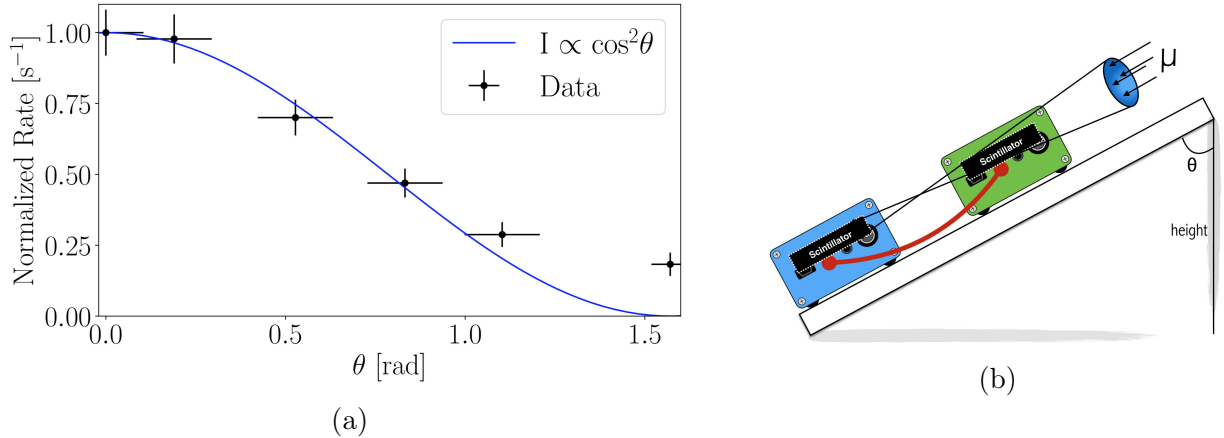


Figure 7.2: The measured cosmic-ray muon angular distribution measured by the coincident detector. The prediction by the PDG is shown in solid blue. From Ref. [47].

As indicated in Sec. 2.1.2, the angular cosmic-ray muon dependence at sea level should follow a cosine squared dependence. The overall measured shape of the distribution is found to agree relatively well with the cosine squared prediction; however, it is shown that the rate does not fall completely to zero in the horizontal configuration ( $\theta = \pi/2$ ). This anomaly appears to be related to showers of particles developing in the roof above the detector, producing a spray of high-energy electrons or photons that can trigger both detectors. Further investigation can be conducted by shielding one of the detectors with a dense material (such as lead or iron) and performing the horizontal measurement a second time. Additionally, doing the measurement near a basement wall can provide additional shielding.

## 7.2 Cosmic-ray muon attenuation in a Subway station

While visiting the Research Center for Neutrino Science (RCNS) at Tohoku University, we noticed that the Aobayama subway station was extremely deep underground and decided to investigate if there was a noticeable change in the muon rate compared to the office where we were working. After spending approximately 30 minutes in the station, we decided to travel to another station (Aoba-Dori Ichibancho station) a bit closer to my hotel to see if the rate changed, and then took a final measurement at ground level.

The muon attenuation was found to be surprisingly pronounced, as shown in Fig. 7.3. We would anticipate this measurement also working rather well in the deep subway stations. Are there any deep subway stations nearby? Washington Park station in Oregon is the deepest at 79m. Forest Glen station in DC is apparently pretty deep as well. If you measured the rate as a function of depth, you could reverse this, and use the detectors to tell you how far underground you are. This is a measurement of what we call overburden. It's often reported in meter-water-equivalent, which corresponds to the amount of water overhead that would be needed to have the same shielding effect.

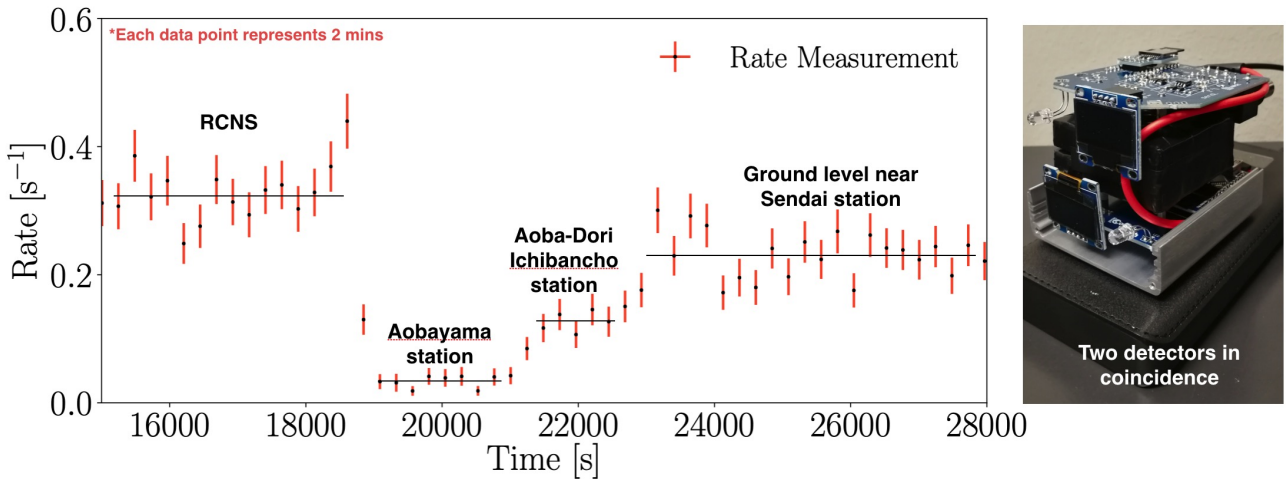


Figure 7.3: Subway in Japan.

There are likely other underground areas in your area from which this measurement can be made. While the cosmic ray muon flux per unit solid angle is from directly above, the largest flux, per unit zenith angle, is actually near 70 degrees. To get a good measurement, you must not only consider the vertical overburden but also the overburden away from vertical.

## 7.3 Electromagnetic component of cosmic-ray showers

We've explored in Sec. 2.1 that at sea level, there exists a flux of electrons and positrons showering down on the Earth. The majority of this flux possesses energies less than 100 MeV, with a minimal contribution above 1 GeV. Subsequently, in Sec. 3.2, we delved into the fact that this electromagnetic component is not particularly penetrating and can be significantly attenuated with a few tens of centimeters of concrete (the radiation length in concrete, as found in Table 3.1, is 10.7 cm). To test this assertion, we can measure the coincidence rate on top of a building and then again several floors lower.

We anticipate minimal attenuation of cosmic ray muons, but a significant reduction in the electromagnetic component. A typical building often features around 15 cm of concrete between each floor. By measuring the vertical muon rate on the top floor and then repeating the measurement 5 floors lower, we expect the electromagnetic component's energy to be attenuated by 7 radiation lengths (a factor of 1000).

Two detectors were placed in coincidence mode, one atop the other, following configuration (c) of Fig. 5.6. They were positioned on the rooftop of the 10-floor WiPAC building for a 24-hour period, enclosed in a plastic bag for weather protection. Subsequently, the same two detectors were relocated to the 5<sup>th</sup> floor, and the measurement was reiterated. The outcomes of this measurement are presented in Fig. 7.4.

The results reveal that the rate on the building's top floor is 27% higher than the measurement made on the 5<sup>th</sup> floor. This discrepancy in rate is presumed to be primarily attributed to the reduction of the electromagnetic component. As elucidated in Sec. 2.1, we elucidate that approximately 33% of the total cosmic ionizing radiation flux at sea level emanates from the electromagnetic component.

We've always entertained the idea of conducting a study by submerging CosmicWatch into a lake. In such a scenario, the level of shielding is precisely defined and is commonly expressed in physics experiments in terms of meter water equivalent (m.w.e.). If you decide to embark on this experiment, ensure that your detectors are enclosed in a water-tight container. An anticipated 30% reduction in the coincident rate is expected within the initial few feet as the electromagnetic component diminishes. Following that, there will be a more gradual decline in the muonic component as you proceed deeper into the water, ideally reaching depths of tens of meters.

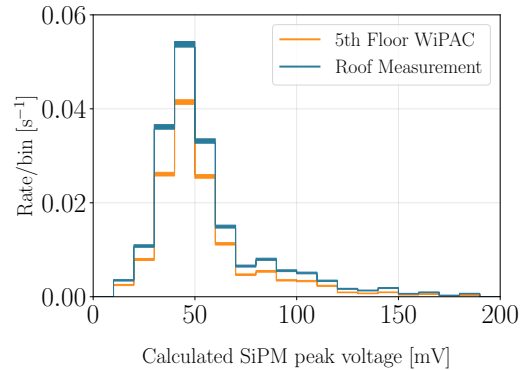


Figure 7.4: The calculated SiPM peak voltage on the roof of the WiPAC building compared to on the 5<sup>th</sup> floor.

## 7.4 Reducing radioactive backgrounds

There is a notable presence of natural radioactivity in the environment that the CosmicWatch detector can detect. Certain items, such as orange FiestaWare plates from 1936-1943 used natural uranium for coloring, exhibit radioactivity (Prof. Axani has a few if you are interested in seeing them). Even common household items like potassium chloride (salt substitute) can produce a signal (requiring approximately 11 oz for detection). Additionally, granite countertops in homes might also exhibit radioactivity, so it's worth checking for.

Shielding against natural radioactivity in the environment can be challenging. Typically, at sea level, the largest component of our signal originates from radioactive backgrounds. Therefore, it is beneficial to explore ways to minimize this background and enhance the purity of the cosmic-ray muon signal (beyond using coincidence mode).

The use of dense materials around the detector can attenuate the incoming flux from background radiation. While an ideal choice would be a radio-pure material, we can illustrate the effect using lead bricks. Six lead ingots (each measuring  $2'' \times 4'' \times 8''$ ) were strategically placed to provide  $4\pi$  coverage around a single detector. The detector recorded data directly to the microSD card over the course of a full day. Subsequently, it was positioned on a workbench in the same room (far away from the lead) to measure the background spectrum for another full day. The resulting calculated SiPM peak voltage for the two measurements is depicted in Fig. 7.5. As anticipated, this setup significantly reduces events contributing to the low SiPM peak voltage region, which is predominantly influenced by radioactive background.

Lab 303 (AxLab) has several led bricks if you would like to use them. Alternatively, you can experiment with different materials, bury the detectors in the ground, or try using water (ensuring the detectors are sealed securely). Explore measuring the effectiveness of various materials of the same thickness and consider why some materials are more effective than others. Additionally, investigate the impact of different thicknesses of shielding.

Another experiment you can conduct involves studying the reduction in rate with distance from a radioactive gamma-ray source. To set up this experiment, you can contact a lab instructors, who have access to radioactive button sources located in Sharp Lab 016A. This experiment provides an opportunity to demonstrate the inverse square law ( $1/r^2$ ) decay associated with ALARA (As Low As Reasonably Achievable) principles, a concept emphasized in radiation safety lectures.

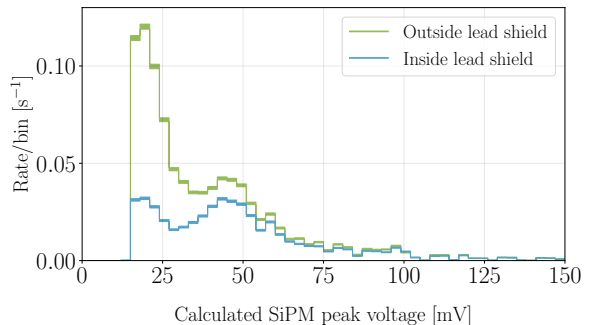


Figure 7.5: The effect of surrounding a single detector in a lead enclosure.

## 7.5 Correlation between the cosmic-ray muon rate and atmospheric pressure

A correlation exists between the atmospheric pressure and the cosmic-ray muon rate. It can be expressed as follows:

$$\frac{\Delta I}{\bar{I}} = \beta \Delta P, \quad (7.1)$$

where  $I$  represents cosmic-ray muon intensity,  $\Delta P$  is the measured atmospheric pressure compared to the average pressure, and  $\beta$  is the barometric coefficient [48]. This correlation is actually the result of several processes outlined in Sec. 2.1.2. The barometric coefficient represents the percent change in detector count rate per hPa change in atmospheric pressure.

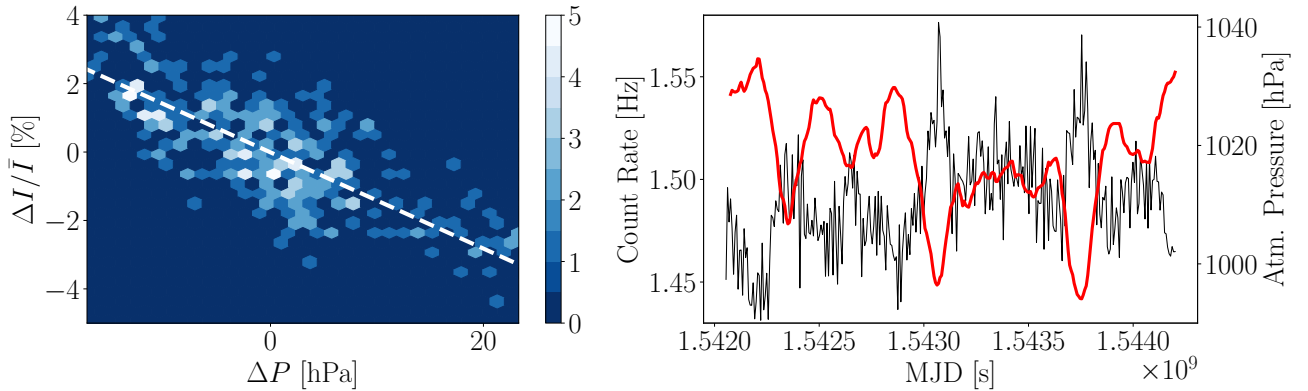


Figure 7.6: Left: The correlation between the atmospheric pressure and the detector count rate. Right: The detector count rate in blue and the atmospheric pressure in red as a function of modified Julian date (MJD). Both plots show the data binned with a bin size of two hours.

For this measurement, we decided to use an array of master-coincident detectors (ten detectors) to improve the statistics. Five pairs of detectors were each connected in configuration (c) of Fig. 5.6, and left to record the cosmic-ray muon rate over the course of 24.8 days (from 13:35 hrs Nov. 12th to 09:00 hrs Dec. 7th 2018.). Data was recorded directly to a microSD card and powered through an 8-way USB hub powered through a wall outlet. Since the CosmicWatch does not keep accurate time over long time-scales, we assume the time drifts linearly with time, and scale the uptime of all detectors such that they are all the same. This is not ideal, and we would recommend recording the data directly to a computer through the `import_data.py` script in the future to get an accurate time stamp on all events. However, this is more prone to losing data, since you would require a computer that runs continuously for a significant amount of time. The array of detectors was placed in the 4<sup>th</sup> floor WiPAC lab in Madison, WI. Atmospheric pressure for Madison was found in Ref. [49]. However, the UD version has a built in pressure sensor if you would like to try using it.

Fig. 7.6 (left) shows the correlation between the detector count rate and the atmospheric pres-

sure. The calculated correlation is shown in the dotted white line. A least squares fit yielded a barometric coefficient of  $-0.141 \pm 0.007 \text{ \%}/\text{hPa}$ , in agreement with Ref. [50].

This may be difficult to do with only two detectors since the statistics will be lower, but it will be interesting to see! You can increase the amount of data you have if you ask a friend to also take data at their location, and you add that to yours.

One of our latest adventures is HurricaneWatch. A meteorology student who is a hurricane-chaser is taking our detectors into the storms she studies. The atmospheric pressure during a hurricane can drop by over 100 hPa, which we hope to be able to see. We will be excited to get this dataset!

## 7.6 A true random number generator?

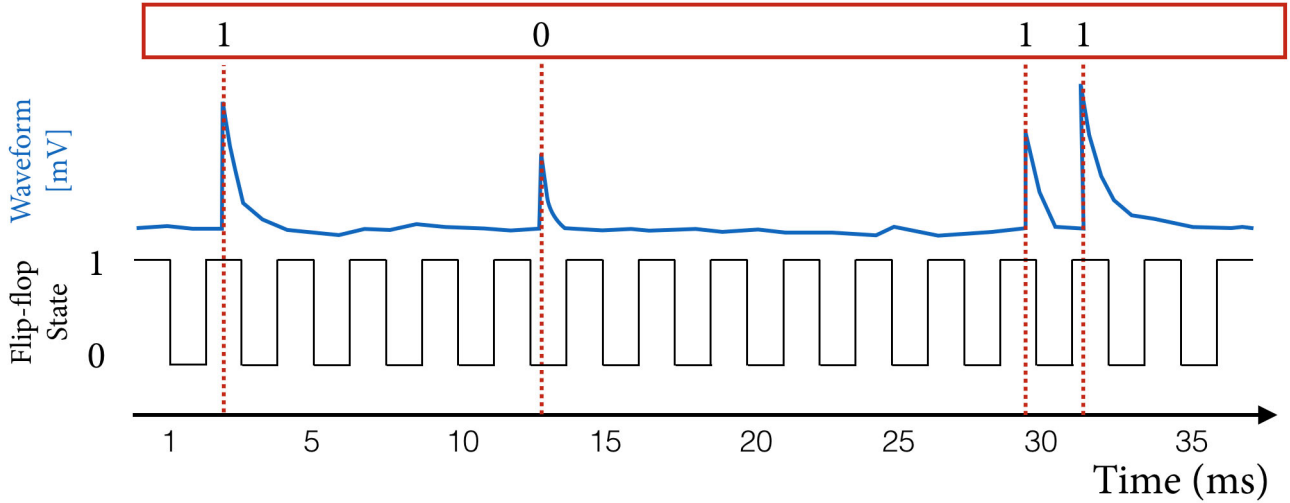


Figure 7.7: An illustrative diagram of the principle behind the random number generator. The x-axis indicates the time measure in milliseconds. Above this, we have the toggle flip-flop, which changes state every millisecond, then an illustrative waveform shown in blue. If the event triggered the detector while in the even state of the flip flop, we assign it a one, otherwise, we assign it a zero. This is shown in the red box at the top of the diagram.

Many applications require random numbers. Often, a random number may be generated through some algorithm, but this, therefore, becomes deterministic since if the user knew the algorithm and starting conditions, they could determine the output. An ideal random number generator would be derived from a truly random process, such as the arrival times of cosmic-ray muons or the radioactive decay of an element. The sum of two random processes will also be random, such as the signal from the radioactive backgrounds in the detector along with the cosmic-ray muon signal. For this measurement, we are following the description found in Ref. [9].

Any number can be expressed in terms of a sequence of ones and zeros; this is known as binary. An  $N$ -length sequence is able to represent a number from zero to  $2^N - 1$  (corresponding to  $2^N$  different values). For example, the 4-bit binary sequence "1011" corresponds to  $1 \times (2^3) + 0 \times (2^2) + 1 \times (2^1) + 1 \times (2^0) = 8 + 0 + 2 + 1 = 11$ .

We can convert the time stamp of a radioactive decay trigger into a "1" or a "0" using a *toggle flip-flop*. The toggle flip-flop is simply a state that changes from one to zero periodically (we will use a frequency of 1 kHz). If a particle passes through the scintillator during an even time stamp (as measured in milliseconds), we assign it a "1"; if it passes through an odd time stamp, we assign it a "0". After  $N$  triggers, we can build an  $N$ -bit random number. This is schematically illustrated in Fig. 7.7.

For this measurement, we use data taken from a 20-day background lab measurement. A single

detector was used. After triggering on a total of  $t$  events, we can build  $t/N$  N-bit random numbers. To illustrate this, if we choose to generate 8-bit random numbers (from 0 to 255), we can plot the number of each occurrence. This is shown in Fig. 7.8.

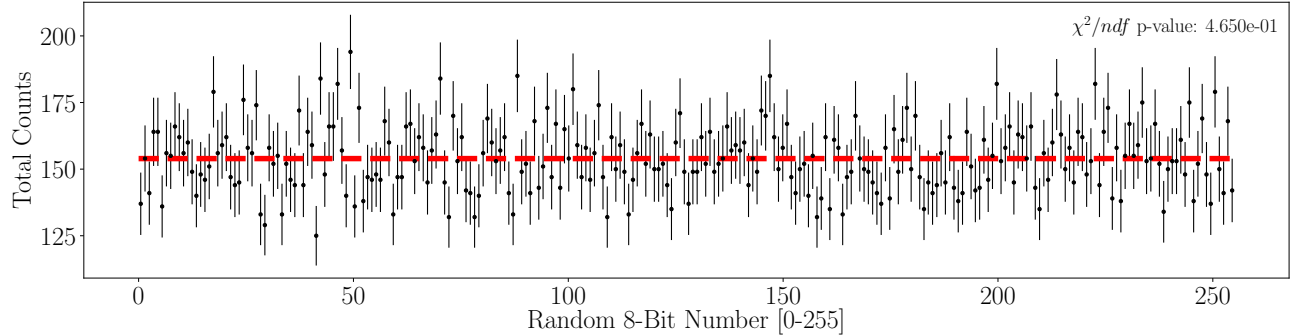


Figure 7.8: The number of occurrences of the generated numbers from 0-255. The reduced  $\chi^2$  p-value assuming that the distribution should be randomly distributed about the average number of occurrences is given at the top right of the figure.

Fig. 7.8 shows the random nature of the triggers. Each number should be equally probable to occur. The reduced  $\chi^2$  indicates a p-value for this assumption shown in the top right of the plot.

In your case, you may consider collecting data from a natural radioactive source. A suitable option is to acquire an 11 oz or larger container of salt substitute (potassium chloride) for this study. The radioactive emissions from the potassium chloride will contribute to a count rate that is higher than the background when the source is placed near the detector.

There are several factors that can introduce bias into the random number generator. Let's consider extreme scenarios. Imagine a scenario where the trigger rate is approximately 1 Hz, and the flip-flop state changes only every 10 seconds. In this case, the first ten triggers would yield all ones, followed by the next ten triggers giving all zeroes. This would result in biased high values for the initial numbers and biased low values for the subsequent ones. This example highlights the need for the toggle flip-flop to change states at a much higher rate than the trigger rate.

Another potential source of bias arises if the microcontroller fails to produce an equal number of even and odd timestamps due to internal configuration issues. For instance, when using



Figure 7.9: Background rate measurement with (left) and without (right) an 11 oz container of potassium chloride. The rates are measured as  $7.2 \pm 0.1$  Hz and  $3.94 \pm 0.08$  Hz, respectively.

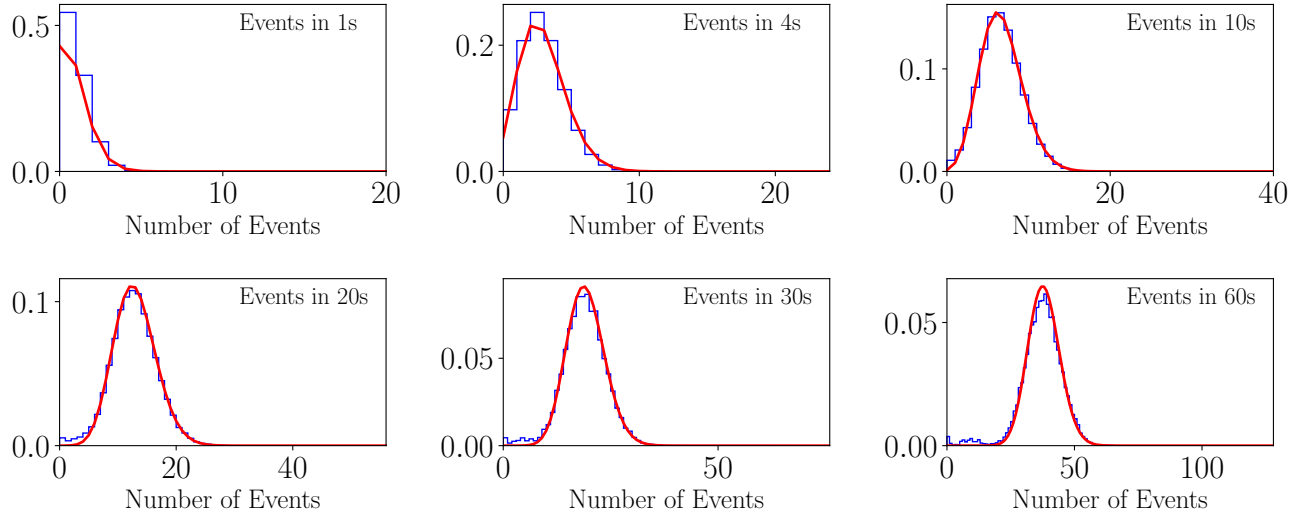


Figure 7.10: The distribution of number of events per unit time. Each cell represents a different amount of time in which the data is binned (labelled on the top right of each cell). The red line is the expected Poissonian distribution from Eq. 5.4.

the microseconds() function in Teensy/Arduino, the reported timestamp may only be accurate to the nearest even microsecond. It is crucial to thoroughly study and quantify the randomness of the data collected.

A funny thought could be to use this idea to turn the detector into a *magic eight ball*.

## 7.7 Gamma-ray spectroscopy

The detection material is primarily composed of polystyrene, a low-density synthetic hydrocarbon. Referring to Fig. 3.4, we observe that for carbon-based materials, at MeV gamma ray energies, the predominant interaction is Compton scattering. Ideally, in gamma ray spectroscopy, capturing the full energy of the gamma ray, as in photoelectric absorption (more common in high-density materials like germanium), is desired. However, in our case, a common interaction involves the original gamma ray undergoing Compton scattering within the scintillator, depositing some energy, and then leaving the scintillator. This results in a smeared energy distribution, lower mono-energetic peaks, and an increased rate in the Compton valley.

While challenging, some information can still be extracted from gamma ray sources, as exemplified in Fig. 7.11. In this context, data was collected with various sources at the MIT Junior Lab. Although we may not be able to discern monoenergetic peaks, interesting features emerge. For instance, Cobalt-60 emits two relatively high-energy gamma rays (1.17 and 1.33 MeV) compared to Cesium-137, which features a dominant gamma ray at 0.66 MeV. It is worth noting that the SiPM peak voltages, serving as a proxy for the number of observed photons and related to the energy deposited by a gamma ray, exhibit variations.

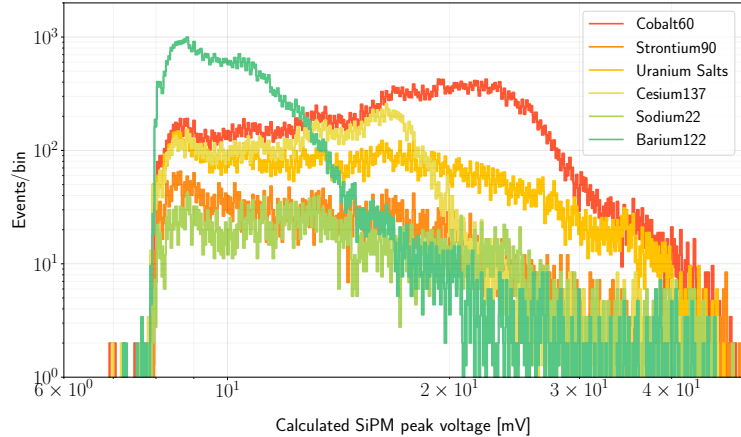


Figure 7.11: The distribution of number of events per unit time. Each cell represents a different amount of time in which the data is binned (labelled on the top right of each cell). The red line is the expected Poissonian distribution from Eq. 5.4.

Gamma ray spectroscopy with these detectors would be enhanced by utilizing a denser material, larger volume detectors, and greater photocathode coverage. We do have dense scintillator crystals if you would like to try.

# Chapter 8

## UNTESTED MEASUREMENTS FOR THE ADVENTUROUS

This section outlines a selection of measurements that we aspire to include in the curriculum in the near future. Opting for one of these measurements means venturing into relatively unexplored territories. We highlight the challenges associated with these measurements, and in the case of the solar flare measurement, success depends on fortuitous timing! Therefore, exercise caution. Nonetheless, if you successfully conduct any of these measurements, they could potentially become part of next year's curriculum! Best of luck!

## 8.1 The velocity of cosmic-ray muons

To reach sea level, cosmic ray muons must travel at relativistic speeds. One way to measure their velocity involves assessing the time delay between their passage through two widely separated scintillation counters.

While the CosmicWatch detectors have a triggering electronics precision in the order of microseconds, limiting the observable travel time differences to distances requiring thousands of feet between detectors, there is a potential approach using an Oscilloscope. By accessing the output of the SiPM inside the detector, you can obtain a signal with a fast rise time. Placing two detectors several feet apart and digitizing both fast outputs using the Oscilloscope might reveal an observable shift.

However, this measurement is challenging due to the limited statistics. To detect a shift of 1ns, the detectors would need to be approximately 1 feet apart. Can you detect a 1ns shift? It might require you to fit the SiPM curve to the digitized waveform to get an accurate time stamp. You could separate them by, say, 12 feet, but you will have small statistics. Could you estimate the rate? At such distances, the coincident rate is low, very low, and the accidental coincidence rate requires careful investigation.

Before attempting this measurement, consider the method you plan to use for recording data. Ideally, you would want the Oscilloscope to save the waveform of all observed coincident events for offline analysis. To assess the feasibility of your setup, you could start by using two BNC cables of different lengths, e.g., 6" and 8". The observable signal travel time difference between these cables, in a coincident event with detectors placed close together, will provide insight into the required detector separation to observe a difference given the Oscilloscope's limited sampling speed. During the actual measurement, ensure that the BNC cable lengths are the same.

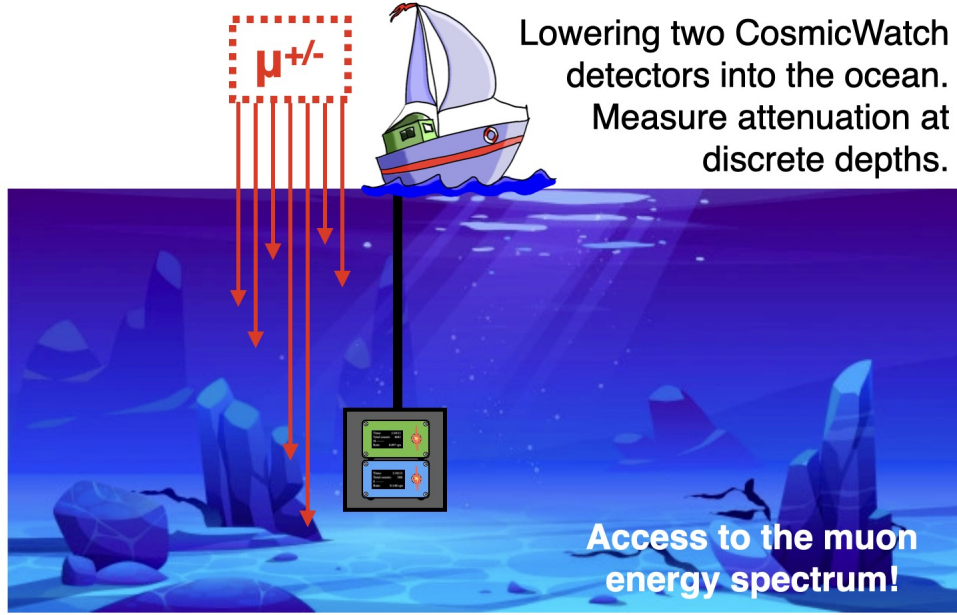


Figure 8.1: Measuring the muon rate as a function of depth underwater should be able to give you the muon rate.

## 8.2 Muon Rate Underwater

Physicists typically report the equivalent overburden in terms of how much water would provide the equivalent shielding. A measurement in actual water can be useful since it provides a homogeneous material and is abundant. We will attempt to measure the attenuation as a function of depth in a deep lake/ocean. Initially, we should observe a steep decrease due to the electromagnetic component dropping out, then a slow decrease as a function of depth. If you frequent a pool, they may let you take data in the deep end. A student at MIT dropped them in the Charles River to measure the attenuation.

It's neat actually. If you could measure how the rate decreases with depth, you should be able to extract the muon energy spectrum. That is, if muons had extremely high energies, they would penetrate deeper into the water. This would be a tricky bit of unfolding, but extremely cool.

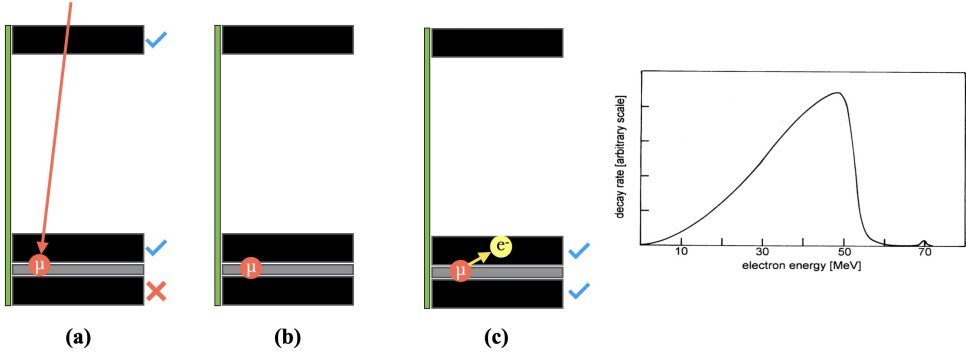


Figure 8.2: (a) A muon passes through the top and middle detector. (b) It hangs out for a bit. (c) the second or third detector observe something 100s of ns to a few microseconds later, as the muon decays to a Michel electron.

### 8.3 Muon lifetime

This is cool. It might be possible to measure the lifetime of the muon. As mentioned earlier in this document, the muon is unstable. Their rest mass is approximately  $207 m_e$ . It has a lifetime of roughly  $2.2 \mu s$ . The fact that muons are sufficiently energetic and decay only under the weak interactions causes that they can reach sea level. When it decays, it emits a two neutrinos (invisible to us), and a fairly energetic electron, called the Michel electron. The Michel electron energy spectrum is shown in Fig. 8.2 right. If you can stop a muon and see how long it hangs around for, you can get the muon lifetime. I think you will need three detectors though. We have a special detector in Lab 303 that might be suitable for this. It's shown in the image below, Fig. 8.2.

With three detectors one-on-top of each other, this measurement should be possible. The top two are used to trigger on an incoming muon. If the bottom detector doesn't trigger, that likely means that the muon stopped in the middle detector. Then you wait. Not long though, since after a few 100s of nanoseconds, the Michel electron should pop out and trigger either the middle or bottom detector. By measuring the time it takes between these two signals, you can infer the muon lifetime by fitting an exponential + constant to the  $\Delta t$  time between trigger and the Michel. The exponential decay constant represents the lifetime of the muon. The constant is there to account for the accidental coincidences, which are independent and therefore will have a constant rate.

## 8.4 Solar flares and the Forbush decrease

At higher altitudes and latitudes, where lower-energy primary cosmic ray particles are observable, a correlation between cosmic radiation and solar activity becomes apparent. Solar flares, often associated with coronal mass ejections, can lead to significant temporary increases in count rates. This effect is more pronounced at higher altitudes, where the Earth's magnetic field offers less protection to GeV cosmic ray particles compared to regions near the equator.

NASA and the National Oceanic and Atmospheric Administration operate the Geostationary Operational Environmental Satellite (GOES), which records the incident particle flux from the sun, including protons, electrons, and X-rays. Publicly available data from GOES can be used to correlate transient solar events with cosmic ray muons. Solar flares are classified using letters A, B, C, M, or X, representing the power per unit area of an event. A numerical suffix (0 to 9) indicates the event's strength; for example, an X2 flare has twice the strength of an X1 flare. Each letter classifies events with an order of magnitude difference between classes, with X denoting the most powerful flare classification. While X-class solar flares are relatively rare, occurring only a few times per year, there's a chance your detector might be active during such an event!

The real-time clock on CosmicWatch detectors is updated each time the software is re-uploaded to the Teensy 4.0. Over time, clock drift may occur, leading to an inaccurate local time stamp. However, this might not be a significant issue since solar flares can have relatively long durations. If clock drift is a concern, data can be recorded directly to the computer, where the computer's time stamp is replaced with the RTC time stamp, providing a more accurate reading.

Roughly one day after a solar eruption, the Earth undergoes a solar storm. A brief increase in the magnetic field is observed, followed by a much more pronounced decrease that persists for several hours. Over the span of a few days, the magnetic field gradually returns to its initial strength. This phenomenon is known as the "Forbush decrease." Initially, the observed cosmic ray radiation intensity starts to decrease.

Given the crucial role of Earth's magnetic field in shielding us from cosmic radiation, this effect should also be observable. As illustrated in Fig. 8.3, the change in rate is at the percent level. Changes at the percent level should be detectable over the course of a day using configuration (d) of Fig. 5.6. However, it's important to note that atmospheric conditions may also influence the measurement, so considering barometric pressure measurements could be beneficial.

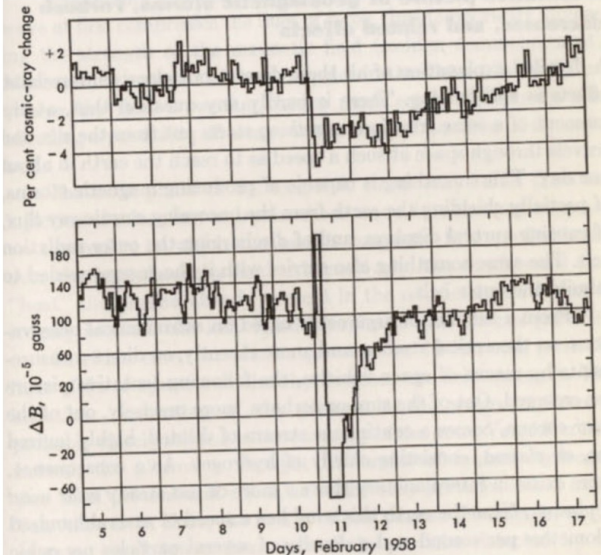


**Fig. 14-2** Typical Forbush decrease. The lower curve represents the horizontal component  $\Delta B$  of the magnetic field measured, from an arbitrary zero, in units of  $10^{-5}$  gauss. The upper curve shows the corresponding variations of cosmic-ray intensity (measured by a neutron monitor in Chicago) as a percentage of the normal intensity. Shown on the horizontal axis is the universal time, in days. (From F. Bachelet, P. Balata, A. M. Conforto, and G. Marini, *Il Nuovo Cimento*, vol. 16, p. 292, 1960.)

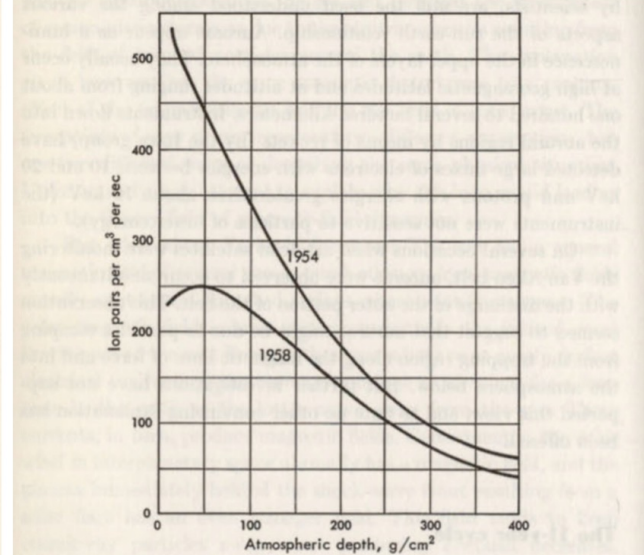


**Fig. 14-3** Intensity of cosmic rays as a function of atmospheric depth, measured at a geomagnetic latitude of  $88^\circ$  N at the time of minimum solar activity in 1954 and at the time of maximum solar activity in 1958. The instrument used was an electroscope; the vertical scale gives the number of ion pairs per second produced by cosmic rays in  $1\text{ cm}^3$  of air at standard temperature and pressure. The horizontal scale gives the atmospheric depth, in grams per square centimeter. (From H. V. Neher, *Nature*, vol. 184, p. 423, 1959.)

Figure 8.3: The Forbush decrease (left) and solar maximum/minimum cosmic-ray flux (right). This figure comes from Ref. [3].

## 8.5 Measuring the air shower size

Air showers were first discovered using coincidence counters, a concept very similar to the one employed in CosmicWatch. An air shower involves multiple particles arriving simultaneously. Such showers can occur when muons interact while traversing material above the detector, such as the building's roof, or, as depicted in Fig. 8.4, a sheet of lead.

The objective of this measurement is to investigate coincident events between two sets of coincidence detectors based on the lateral distance between the two sets. The challenge lies in the potential requirement for 3 to 4 detectors, as illustrated in Fig. 8.4. Two sets of coincidence detectors (totaling 4 detectors) would yield a lower accidental coincidence rate compared to using 3 detectors (excluding detector C). While the detectors are not configured to record triple coincidences via the microSD card, connecting all detectors to a single computer (via a USB hub) allows the data from each detector to be saved in a unified file using the `import_data.py` script. The timestamps from the computer data can then be analyzed to identify coincidence events.

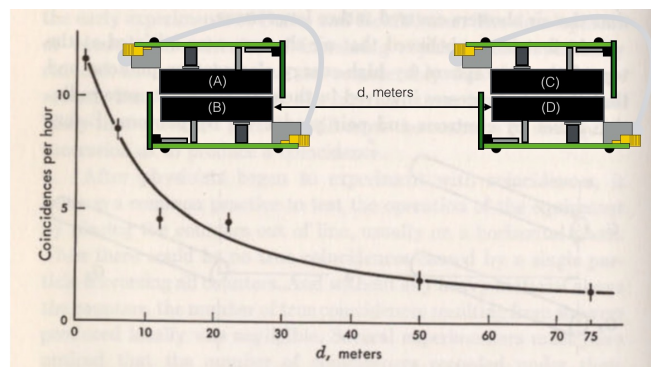


Figure 8.4: Recommended configuration for measuring air shower size. Data from Ref. [3].

# Chapter 9

## FUN MEASUREMENTS WE HAVE DONE

You will not be able to do the set of measurements we describe here. However, they are fun to read about. And they may inspire ideas so you can make some fun measurements too!

### 9.1 Measuring the cosmic-ray muon rate in an airplane at 33,000 ft

A rate measurement was conducted during a flight from Boston International Logan Airport (BOS, latitude =  $42.4^\circ$ ) to Chicago O'Hare Airport (ORD, latitude =  $42.0^\circ$ ) using a single detector. The data was recorded onto a microSD card and powered by a 10,000 mAh USB power bank. The altitude of the airplane was obtained from flight records available on FlightAware.com [51].

Fig. 9.1 (left) illustrates the detector's trigger rate in blue as a function of time, binned into 60-second intervals. The error bars depicted are solely statistical. Airplane altitude data were linearly interpolated between points to estimate the altitude at any given minute. The interpolated altitude data were fitted to the detector data using a simple exponential plus an offset. Since the absolute take-off time was unknown (data recorded to the microSD card), we allowed the altitude timestamps to shift during minimization. The best-fit equation is displayed at the top left of this figure, where  $\text{ALT}[t]$  represents altitude measured in kilometers as a function of time. The best-fit is also presented as a dashed red line.

Fig. 9.1 (right) displays the measured trigger rate as a function of true altitude. Here, we extend the exponential fit beyond the measured values. The count rate uncertainties were calculated by taking the square root of the sum of all events measured at a particular altitude. It's important to note that this data was collected with a detector in master mode, making it sensitive to background radiation from the interior of the plane.

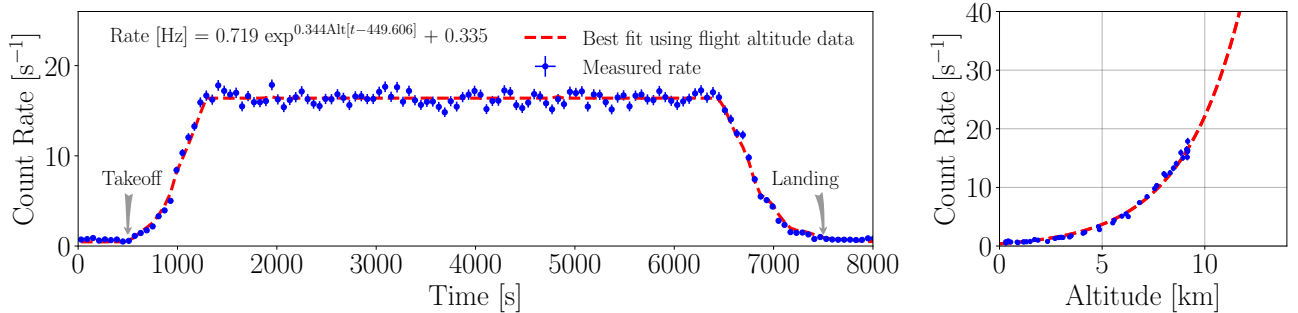


Figure 9.1: (Left) The count rate measured during a flight from Boston to Chicago as a function of flight time. The dashed red line shows the actual amplitude of the airplane [51] scaled by a fitted exponential shown at the top left of the plot. (Right) The measured count rate as a function of altitude. The dashed red line shows the fit.

The cosmic-ray muon flux is recognized to vary with latitude, a variation we have sidestepped by measuring the flux at a nearly constant latitude. Additionally, we anticipate the exponential fit to become less reliable as we extend to higher altitudes, owing to the alteration in flux composition near the primary cosmic ray interaction region.

## 9.2 High altitude balloon measurement at 107,000 ft



Figure 9.2: An image from the high-altitude balloon flight at 107,000 ft. Photo from *Daniel Kaczmar - DNF Systems*.

As mentioned in Sec. 2.1, primary cosmic rays interacting in the upper atmosphere produce showers of particles, some of which decay to muons. Muons are typically produced near an

altitude of 15 km. At higher altitudes, there is an increase in the contribution from other ionizing particles, primarily from electrons/positrons and protons.

During the NearSpace2018 conference [52] in Torun, Poland, we participated in a high-altitude balloon (HAB) flight to measure the ionizing radiation flux as a function of altitude. Two detectors were used for the flight, allowing measurement of both the total rate on the master detector and the down-going rate on the coincident detector. The detectors were placed one-on-top of another (configuration (d) in Fig. 5.6) and taped together to ensure their orientation relative to each other remained constant throughout the flight. The BNC connectors and the OLED screens were removed from the PCB to reduce weight. An 8" 3.5 mm audio cable was used to connect them into coincidence mode, and the SDCard.ino code was uploaded to both detectors. An image of the two detectors is shown in Fig. 9.3. Both detectors were powered by a single-cell lithium-ion battery.

The temperature during the ascent was expected to reach  $-60^{\circ}\text{C}$ , requiring thermal protection for both the battery and to minimize the effect on the SiPM described in Sec. 4.1. A  $10 \times 10 \times 10 \text{ cm}^3$  Styrofoam enclosure with a wall thickness of 1 cm was constructed to house the components. It was large enough to accommodate the two detectors, a small heating element, and two single-cell lithium-ion batteries (one to power the detectors and the other to power the heater). A micro-switch was connected to the battery and wired outside the enclosure so that we could initialize the detectors from outside the enclosure just before the flight.

The HAB was launched on September 22<sup>nd</sup>, 2018, at 12:53 pm. DFN System recorded the balloon altitude and location using on-board GPS, and they mounted a camera to the balloon that looked down at the payloads. An image near the maximum altitude of the flight is shown in Fig. 9.2. The master (orange) and coincident (green) detector count rate, binned into 60-second intervals, is shown in Fig. 9.4, along with the altitude data from the GPS (black).

The shape of the measured spectrum in Fig. 9.4 corresponds to the Pforzheim curve. We find an initial maximum count rate (Regener-Pforzheim maximum) for the master detector at an altitude from approximately 16-23 km, around 70-95 minutes into the measurement. After the balloon popped (at minute 118), the detectors fell through the Regener-Pforzheim maximum. The decrease in the trigger rate after passing the maximum occurs due to the detectors ascending beyond the primary interaction region.

The coincidence detector shows a flatter maximum at an altitude from approximately 12-25 km.

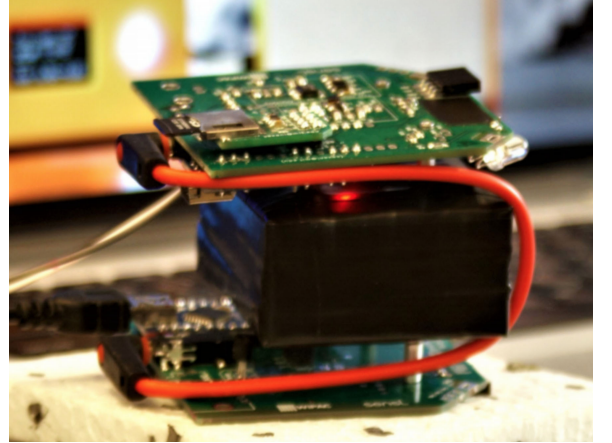


Figure 9.3: The two detectors flown in the HAB flight. The scintillators were taped together in order to preserve the detector orientation relative to each other.

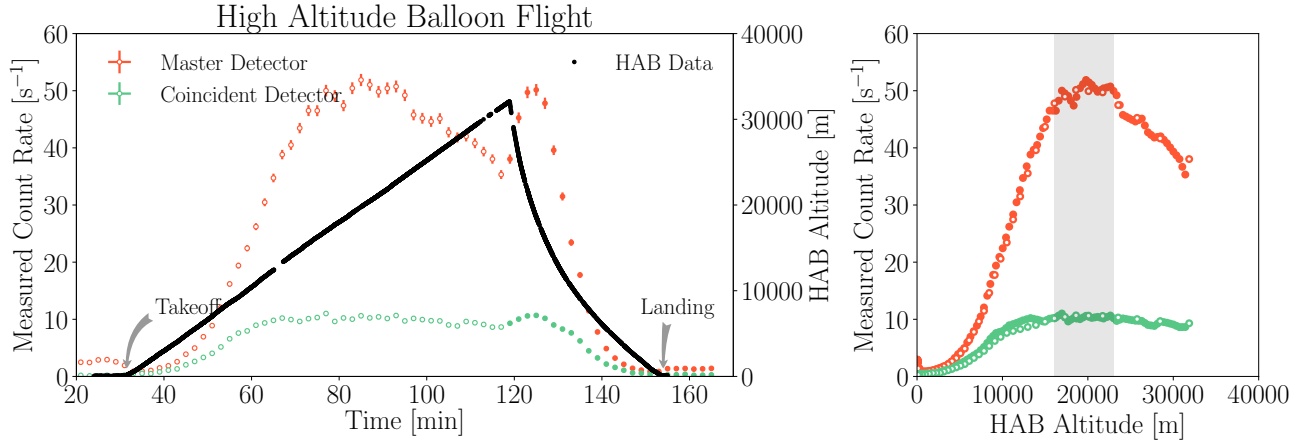


Figure 9.4: (Left) The measured trigger rate for the master (orange) and coincident (green) detector during the high-altitude balloon flight. Take-off occurred 30 minutes after powering on the detectors. The black data points correspond to the altitude as measured through the on-board GPS. (Right) The GPS altitude as a function of trigger rate. The uncertainty in both these plots are statistical.

The peak begins at lower altitudes since we are now preferentially triggering on vertically down-going particles. As described in Sec. 2.1.2, primary particles entering the Earth’s atmosphere at larger angles from the zenith will interact at higher altitudes. In agreement with the data.

### 9.3 Muon rate measurement while flying to the South Pole

In December 2018, I flew to the South Pole as part of a field team to perform maintenance and upgrades on the IceCube Neutrino Observatory [53]. During the flight, I measured the ionizing radiation with two detectors oriented in configuration (d) of Fig. 5.6. Data was recorded to the microSD cards and powered through a single 30,000 mAh power bank.

The first four flights (from Madison, WI USA to Christchurch, New Zealand) were operated by United Airlines and New Zealand Airlines. The altitude data was publicly available for these flights on FlightAware.com [51]. The flight leaving from Christchurch New Zealand, to McMurdo Antarctica, was on a C-17 military jet operated by the US Air Force. Similarly, we flew on a C-130 Hercules, the day after to the South Pole. Since these were military flights, the altitude of this flight was not available; however, several altitude measurements on the second flight were made using GPS. We landed several days later on the 2820 m thick South Pole glacier, approximately 0.5 km from the actual Geographical South Pole.

The full master and coincident detector data are shown in Fig. 9.6, with descriptions of each flight in the text boxes. To give perspective for other measurements, the total data collected by



Figure 9.5: Leaving McMurdo Station, Antarctica on a C-130 Hercules for the South Pole Station.

the master detector was about 50 Mb, whereas the coincidence detector was approximately 15 Mb.

Fig. 9.6 illustrates several very interesting properties. First, there is a trend towards lower count rates near the equator. This is due to the latitudinal variation in the cosmic-ray flux described in Sec. 2.1.2. This effect is most obvious in the flight from SFO to ACK (labeled as flight 3 in Fig. 9.6), which traveled at nearly a constant altitude and a constant rate of latitude change from  $+32^\circ$  to  $-32^\circ$ . We see that the rate is not symmetric. This is because the magnetic latitude is offset from the geographical latitude, which in turn is because the magnetic field is not symmetric about the equator. Second, it's interesting to see that when we landed at the South Pole, there is a noticeable change in trigger rate due to the combination of the elevation and change in Earth's magnetic field.

While flying through the equator at 35,000 ft, I also performed an East-West measurement using configuration (e) of Fig. 5.6. We measure a count rate coming from the east of  $0.69 \pm 0.02$  cps, while from the west  $0.84 \pm 0.03$  cps. This represents a  $22.2 \pm 7.4\%$  increase in the westward direction. This is due to the east-west asymmetry described in Sec. 2.1.2.

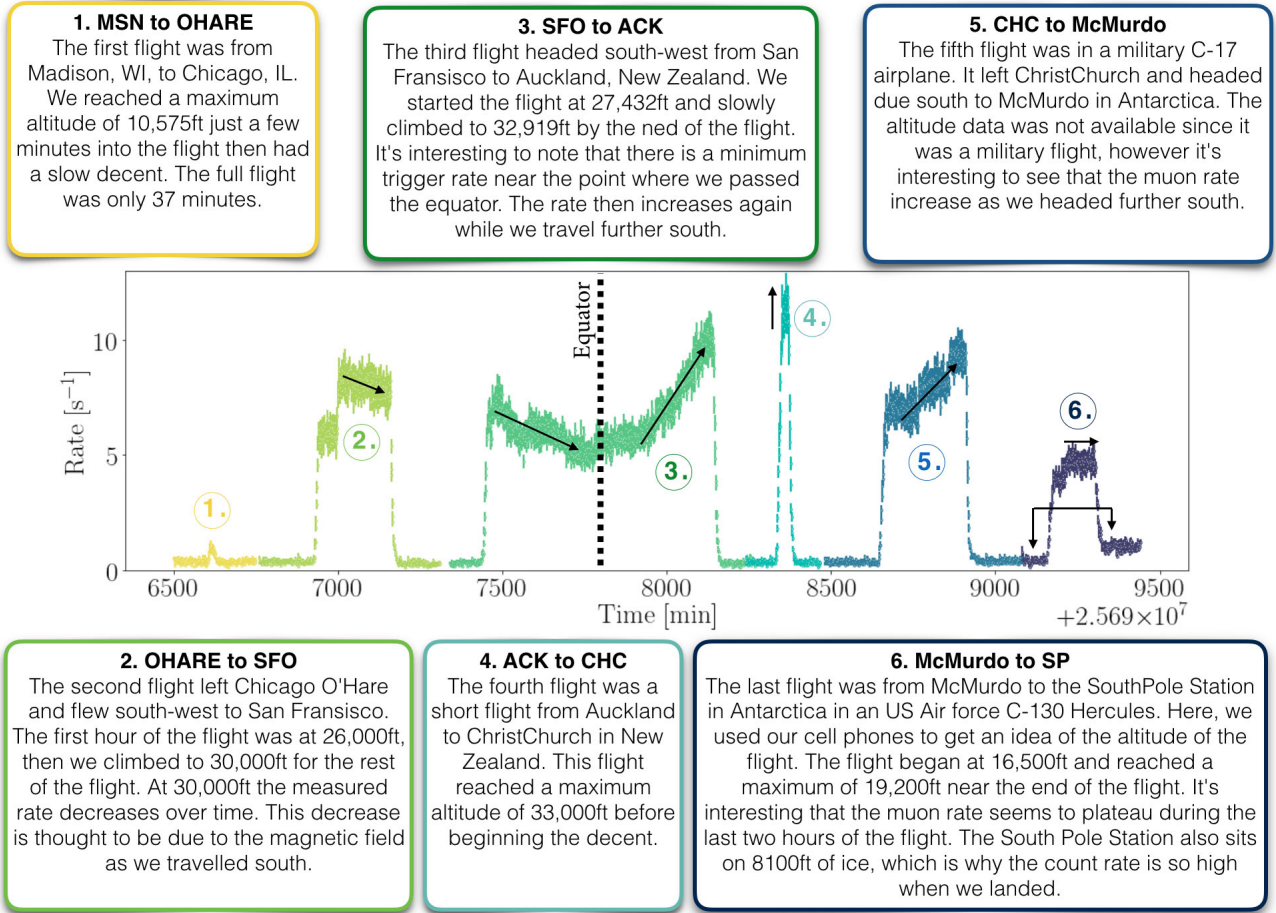


Figure 9.6

## 9.4 Latitude correction to the cosmic-ray muons

We observed latitudinal variation in the cosmic-ray muon rate in the previous measurements. This was an expected effect due to the change in the Earth's magnetic field as a function of latitude. Here, we will empirically attempt to account for the variation in the latitude and altitude based on the previous measurement. We will assume that the change in the rate as a function of latitude follows a sine-squared form, where the minimum occurs near the equator and the maximum occurs near the poles.

$$R[Hz] = N \exp^{\alpha(\sin(LAT[t]+\theta)^2+\beta) \times ALT[t]} - b \quad (9.1)$$

Here,  $\theta$  represents a phase that offsets the latitude to account for the difference between the geographical latitude and the magnetic latitude,  $\beta$  is a factor that permits an altitude effect at the magnetic equator (set the sine term to zero),  $\alpha$  is a scale factor that dictates the strength of

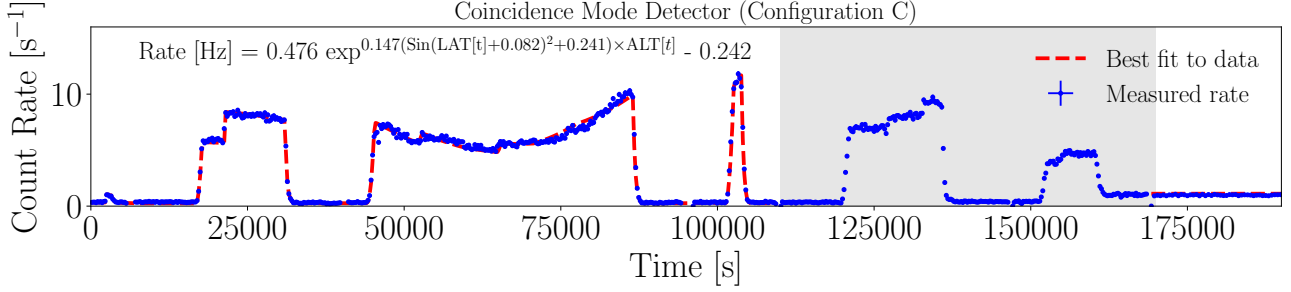


Figure 9.7: The fitted data based on the altitude and latitude data from the first four flights. The fit also includes a measurement after landing at the South Pole, where the altitude and latitude were known (2700 m and  $-90^\circ$ ). The two military flights were not included in the fit.

the latitudinal and altitude effect,  $N$  is a normalization that sets the scale for the exponential component, and  $b$  is an offset that accounts for constant background radiation.

Figure 9.9: Caption goes here.

Fig. 9.9 uses the function in Eq. 9.1 to fit the data for the first four flights, plus the data after landing at the South Pole. The best fit values are shown at the top left of Fig. 9.9. Using this result, we can then invert Eq. 9.1 to calculate the altitude of the two military flights (assuming we flew at a constant velocity directly south). The calculated altitude is shown in Fig. 9.8 for the military flights in green, as well as the measured altitude from GPS in red.

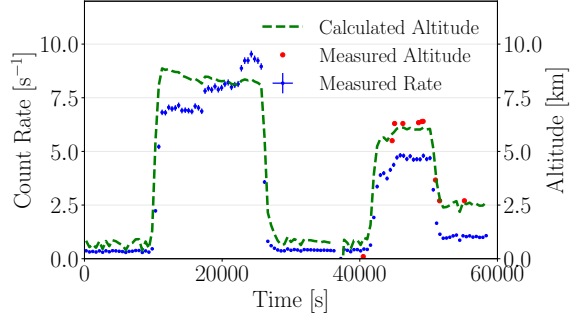


Figure 9.8: The measured muon rate in blue along with the calculated flight altitude in green. The red markers show the few GPS altitude measurements during the flight.

## 9.5 Rate measurement 1 km underground at Super-Kamiokande



Figure 9.10: Dr. Katarzyna Frankiewicz floating in the inner detector of Super-Kamiokande during the Gadolinium upgrade 2018.

Two Desktop Muon Detectors were brought to the Kamioka Observatory located 1 km underground in the Mozumi Mine, Japan. This mine is home to several high profile experiments, perhaps most notably the 2015 Nobel prize winning particle physics experiment, Super-Kamiokande. Two detectors were placed in the Super-Kamiokande control room for 8 hours, and connected together via a 6-inch 3.5 mm audio cable in configuration (c) of Fig. 5.6. The data was recorded from the coincidence detector through the `import_data.py` script directly to a laptop. Using the same detectors and set-up, a rate measurement was also performed outside the Kamioka mine in the observatory dormitory and in the airplane at 36,000 ft when travelling between Warsaw to Tokyo. Fig. 9.11 shows the trigger rate of the coincident detector for these three measurements, as a function of calculated SiPM peak voltage.

The total number of measured coincident events inside the Super-Kamiokande control room was found to be 101. It was observed that 96% of these events were located below the 50 mV peak described in Sec. ??, indicating that these are likely not minimum ionizing cosmic-ray muons.

The average rock density in the mine was measured to be  $2.7 \text{ g/cm}^3$ , corresponding to approximately 2,700 m.w.e. (meter-water equivalent) of overburden [7]. Based on this, we expect the cosmic-ray muon rate to be attenuated by a factor of  $10^5$  compared to a ground-level measurement. With this assumption, we only expect approximately 0.04 cosmic-ray muon events over

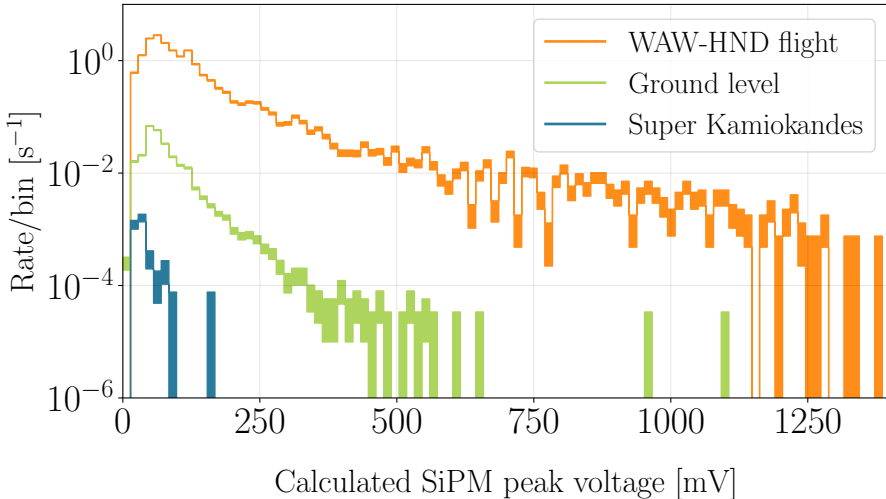


Figure 9.11: The measured coincidence rate at three locations. Data from Ref. [47].

the 8-hour measurement in the Super-Kamiokande control room.

The master detector count rate did not significantly change when it was brought into the mine, indicating that the radioactive background was still present in the control room. Given that the master detector count rate was 1 Hz, Eq. ?? suggests that we should expect 1-2 accidental coincidence events over the 8-hour period (see Sec. 7).

One unaccounted background (briefly mentioned in Sec. 3.3) consists of events in which a gamma-ray from a radioactive decay Compton scattered off the scintillator of the master detector, and then deposited sufficient energy in the coincident detector scintillator. This is thought to be the dominant source of triggers in this dataset, and a Monte Carlo simulation is currently being developed to investigate this. If these events originate from Compton scattering, we can estimate the rate for these types of events. Given the 101 events (with 1-2 assumed to be accidental coincidences and cosmic-ray muons), the calculated accidental Compton scattering coincidence rate in configuration (c) from Fig. 5.6 is found to be  $0.0038 \pm 0.0004$ . A second 8-hour run was performed using the same configuration and location, which found 92 events (with a similar SiPM peak voltage spectrum) corresponding to a count rate of  $0.0035 \pm 0.0004$ .

This result could be further investigated by repeating the measurement, this time with a thin piece of lead between the scintillators. Lead, being a dense material, is likely to either absorb the gamma-ray or absorb some of the energy from the gamma-ray through Compton scattering. Both processes would reduce the probability of measuring the event with the coincident detector. Another potential source for these events is correlated noise. If the lead does not alter the coincident count rate, this is a potential source for this signal; however, thus far, we have not found any evidence of events due to noise.

## 9.6 Portable trigger system for an accelerator beamline

This measurement was previously described in Ref. [47] and represents a practical use for the Desktop Muon Detectors.

A single detector, powered by a 10,000 mAh USB power bank, was placed in the Fermilab M-Test facility to trigger on secondary particles (GeV-scale pions and electrons) from the Main Injector. The purpose of this was to trigger a downstream data acquisition system for another experiment. The BNC output at the back of the detector is the raw SiPM pulse, which has a rise time of a few nanoseconds and a decay time of roughly  $0.5\ \mu\text{s}$ . This signal is useful for experiments that want to use a scintillator but require tens of nanosecond timing. The BNC output was connected to an 80 ft BNC cable to a NIM (Nuclear Instrument Module) rack. The signal passed through a  $\times 10$  amplifier and into a discriminator. If the amplified signal was above a certain value, a binary signal was sent to an AND gate, where it was compared against another scintillator paddle trigger that was located on the other side of the other experiment. If the AND condition was satisfied (i.e., the particle passed through both the scintillator paddle and the Desktop Muon Detector), a binary signal was sent to the data acquisition system that began the recording of data of the downstream experiment. Fig. 9.12 shows the trigger rate of the detector placed in the beamline as a function of time. The beam spills occur every minute for two seconds.

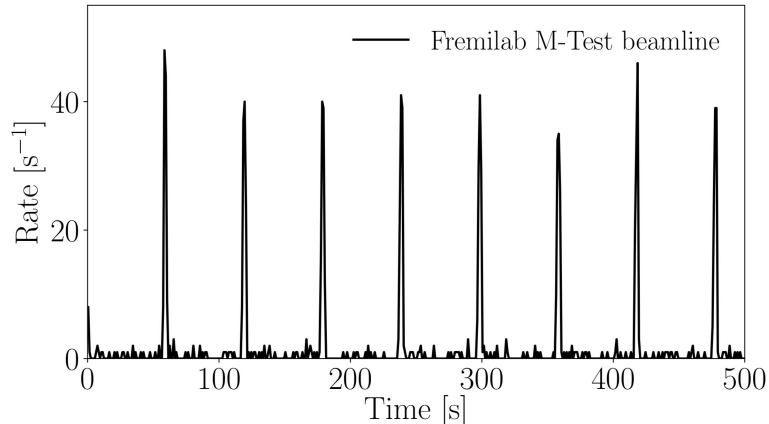


Figure 9.12: The trigger rate as a function of time of a single detector placed in the Fermilab M-Test beamline. Here, the detector is triggering primarily on GeV-scale pions and electrons from the Fermilab Main Injector.

The detector was identified as a useful beamline trigger due to its simplicity. This capability was facilitated by incorporating a BNC output directly connected to the SiPM. For this measurement, the approximate 10 ns uncertainty in the trigger was deemed acceptable. However, if users desire to utilize the FAST output of the SiPM for single nanosecond precision, the SiPM PCB could be modified. We plan on investigating this sometime in the future.

# Chapter 10

## FUTURE MEASUREMENTS

This section compiles a list of potential future experiments that we intend to perform. After gather and analysing the data, these will be added into Sec. 7.

1. **cosmic-ray muon rate at different floors of a large concrete building:** Large concrete buildings, like FermiLab would be great to measure the floor to floor vertical attenuation.
2. **Special relativity measurement:** A repeat of the measurement that confirmed special relativity by measuring the muon rate on top and at the bottom of a mountain. This can be demonstrated using the altitude data here; however, climbing a mountain would make a good story.
3. **Thin lead measurements.** Thin lead sheets, above the coincidence detectors will actually cause an increase in the count rate. This is due to the muon creating a shower of secondaries, that spread out and are able to trigger the detectors simultaneously. After a few inches of lead, the shower is attenuated.
4. **Clean room background measurement.** Background measurement in clean room at SNO+, also a coincidence measurement.
5. **Measure the Southern Atlantic Anomaly.** This could be performed by flying from Mexico to northern Africa.
6. **Extreme weather events:** Measure muon rate during a low pressure event – like a hurricane.
7. **Solar flare events:** Capture data during an intense solar flare.
8. **Solar activity:** There is an 11-year due to the solar activity that modulates the low-energy cosmic rays.

# Chapter 11

## PROGRAMMING THE MICRO-CONTROLLER

This section will talk about the steps to upload the code onto your microcontroller Raspberry pi pico. Once the code is uploaded, cosmic watch is ready to function, and you can take all fun measurements you want!

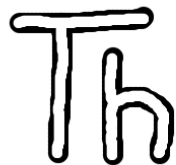


Figure 11.1

## 11.1 Install Thonny

Thonny is an Integrated Development Environment (IDE) for Python programming language. It's designed with beginners in mind, offering a simplified and user-friendly interface for writing, running, and debugging Python code. We will be using this environment to upload the code.

- Step 1: To download Thonny, visit the Thonny website.
- Step 2: Plug in your cosmic watch to your system via a communication cable while holding the bootsel button on the pico.
- Step 3: Once your system identifies the pico open thonny and click on Run and select configure interpreter.
- Step 4: Select "MicroPython (Raspberry Pi Pico)" for the kind of interpreter for thonny.
- Step 5: On the same window, click on install or update MicroPython on the bottom right. That will open another window.
- Step 6: Choose the variant to be Raspberry Pi Pico/ Pico H, essentially the first option and then click on install. Once it's done you may close the interpreter window. You are all set to upload the code.
- Step 6: Download the code this github repository Codever and open it with thonny.

# Chapter 12

## CONCLUSION

The CosmicWatch Desktop Muon Detectors offer a versatile platform for exploring diverse natural phenomena. This document provided a comprehensive overview of the underlying physical processes influencing the detectors and demonstrated how valuable insights can be derived from the collected data. The detectors can be employed to investigate a wide range of phenomena related to the geomagnetic field, atmospheric conditions, cosmic-ray shower composition, particle attenuation in matter, radioactivity, and statistical properties of Poisson processes. Students are encouraged to further develop the concepts introduced or design their experiments. Feedback is highly welcomed to enhance and refine this manual. Enjoy your exploration with the CosmicWatch detectors!

# Appendix A

## DESCRIPTION OF THE CIRCUIT

This chapter elucidates the philosophy behind the analog electronics designed to extract information from the SiPM. The amplitude of the SiPM pulse is directly proportional to the total number of photons striking the SiPM's photocathode. Hence, the objective of the analog electronics is to mold the pulse in a way that enables the slow inexpensive microcontroller to measure certain parameters associated with the pulse amplitude.

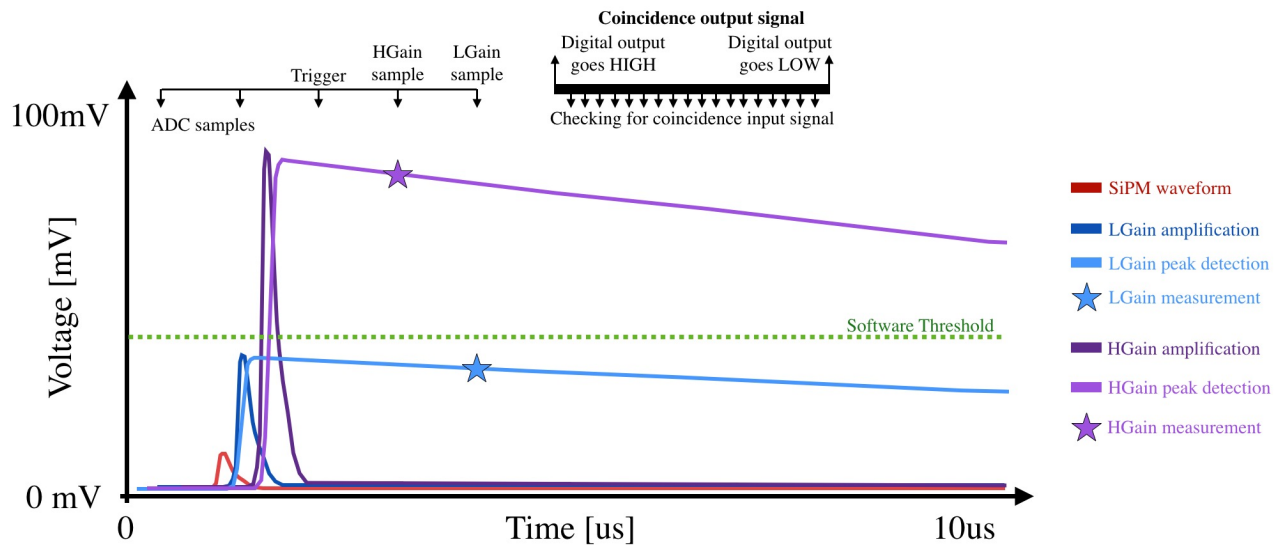


Figure A.1: A description of the analog circuitry and CPU routine. The SiPM pulse (red) is amplified (dark blue), from which we amplify for the high gain channel, and

Fig. A.1 illustrates the four stages of the analog electronics. The SiPM pulse (depicted in red) undergoes an initial amplification of approximately 15 times (shown in dark blue), constituting the low gain amplification section. The low gain amplification signal is then directed into two circuits: a peak detection circuit (depicted in light blue) and a second amplification stage

(depicted in dark purple). The peak detector circuit retains the peak value for a sufficient duration, allowing the microcontroller to measure a single value (indicated by the light blue star). The measured ADC value at this point represents the Low Gain measurement. The second amplification stage further amplifies the pulse by a factor of 7, leading to another peak detection circuit (depicted in dark purple). The dark purple star signifies the High Gain measurement.

At the top of Fig. A.1, an approximation of the routine executed by the CPU is presented. The ADC continuously samples the high gain peak detector circuit until an ADC value surpasses the signal threshold (indicated by the green line), labeled as "Trigger" in the figure. The subsequent ADC sample is employed for the High Gain measurement, while a separate ADC channel samples the Low Gain circuit. A single ADC sample takes approximately  $1.3\mu\text{s}$ . Following the measurement, the coincidence output goes HIGH, and the digital input from the coincidence detector is probed multiple times. The observation of a HIGH digital input is considered a coincident event. The number of probes on the digital input defines the coincidence time window. Subsequently, the digital coincidence output goes LOW.

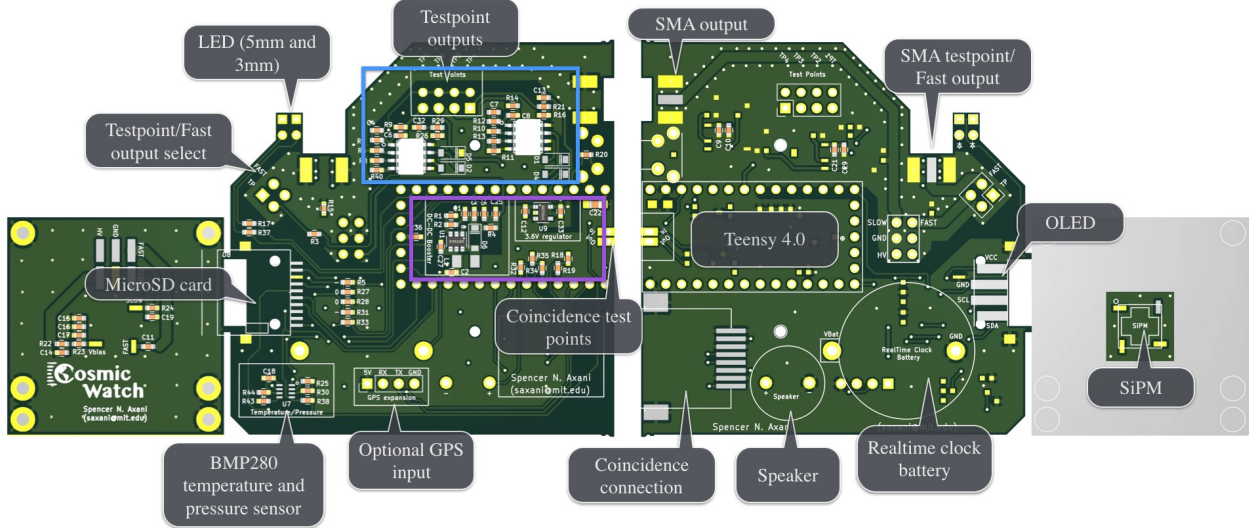


Figure A.2

Fig. A.2 displays the printed circuit boards (PCBs) utilized in the v3 detector. The left (right) side showcases the bottom (top) of the PCBs. The PCB comprises two distinct pieces: the SiPM PCB and the Main PCB. Each component of the circuitry is appropriately labeled. The blue box denotes the analog circuitry, as described previously, while the purple box represents power handling. This includes a DC-DC booster that elevates the 5V voltage from the USB connection to 28.9V and a 3.6V regulator to supply power to the op amps used in the analog circuitry.

Fig. A.3 is provided to illustrate the internal components of the detector. In certain cases, it is preferable to measure the full-sky muon rate. This is most effectively achieved by situating the scintillators between two detectors as closely as possible, as depicted in Fig. 5.6 (d). If your

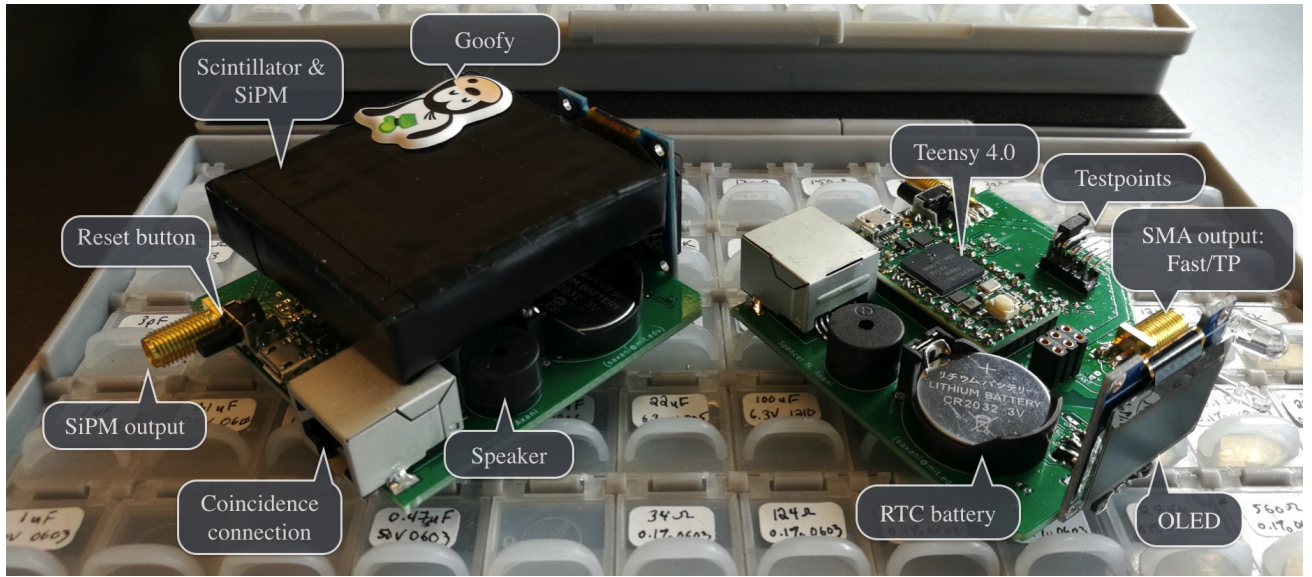
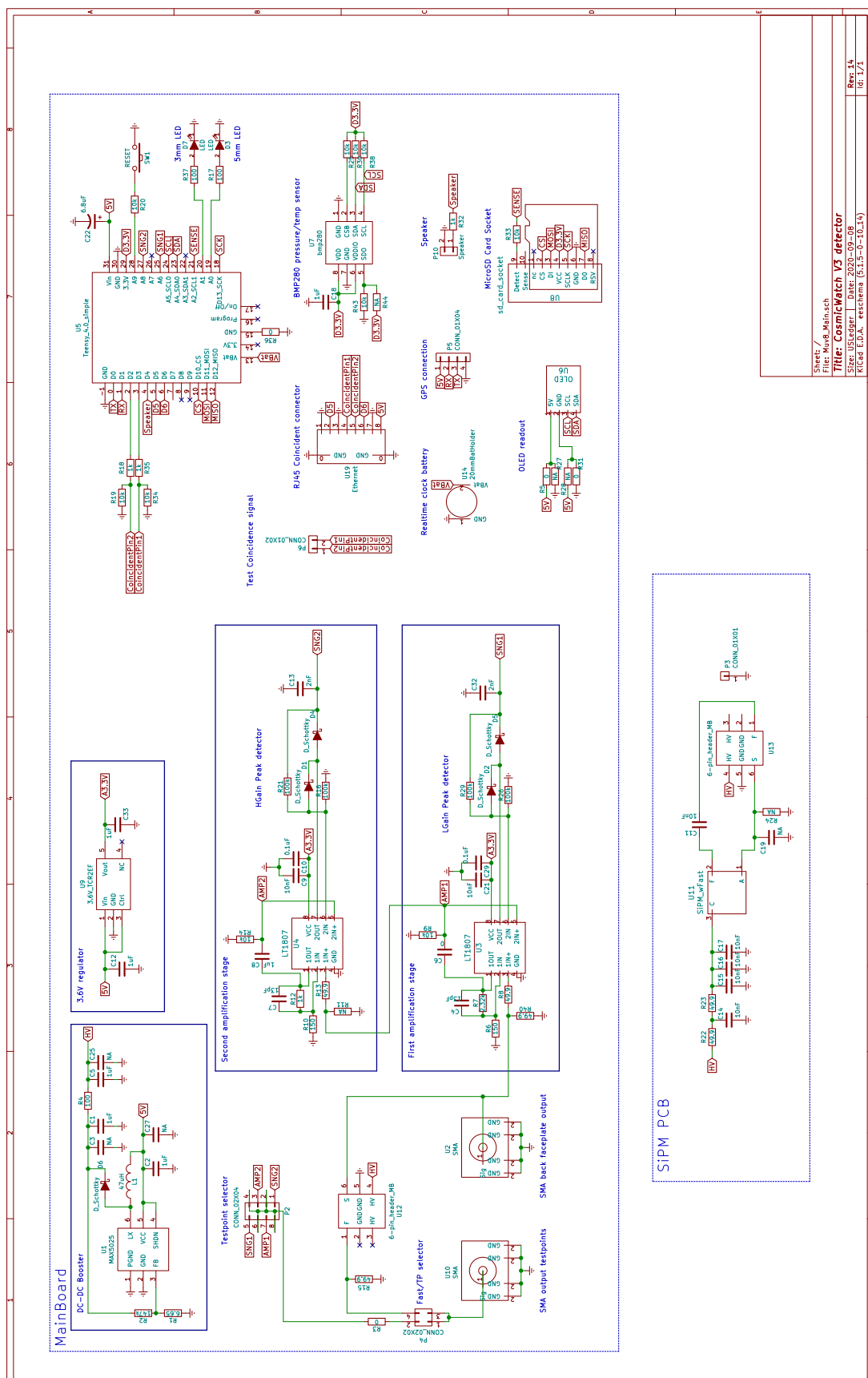


Figure A.3: Image of the detectors removed from the cases.

measurement aligns with this configuration, you may choose to remove the detectors from their cases.

The last figure in this section, Fig. A.4, presents a vector image of the complete circuit. If you have any questions, please feel free to reach out to Spencer at [saxani@mit.edu](mailto:saxani@mit.edu), as we will forgo a detailed description here.



76  
Figure A.4

# Bibliography

- [1] K. O. et al, “Cosmic rays - particle data group,” *Nuclear Instruments and Methods in Physics Research Section A: Accelerators, Spectrometers, Detectors and Associated Equipment*, vol. 38, no. 090001, p. 6, 2014.
- [2] S. K. LBNL, “32. passage of particles through matter,” 2017.
- [3] B. Rossi, “Cosmic rays,” 1964.
- [4] M. W. Friedlander, *A thin cosmic rain: Particles from outer space*. Harvard University Press, 2002.
- [5] P. K. Grieder, *Cosmic rays at Earth*. Elsevier, 2001.
- [6] T. K. Gaisser, R. Engel, and E. Resconi, *Cosmic rays and particle physics*. Cambridge University Press, 2016.
- [7] M. Fukugita and T. Yanagida, *Physics of Neutrinos: and Application to Astrophysics*. Springer Science & Business Media, 2013.
- [8] W. R. Leo, *Techniques for nuclear and particle physics experiments: a how-to approach*. Springer Science & Business Media, 2012.
- [9] C. Grupen and B. Shwartz, *Particle detectors*, vol. 26. Cambridge university press, 2008.
- [10] D. Bird, S. Corbató, H. Dai, B. Dawson, J. Elbert, T. Gaisser, K. Green, M. Huang, D. Kieda, S. Ko, *et al.*, “Evidence for correlated changes in the spectrum and composition of cosmic rays at extremely high energies,” *Physical review letters*, vol. 71, no. 21, p. 3401, 1993.
- [11] G. Taubes, “Pattern emerges in cosmic ray mystery,” *Science*, vol. 262, no. 5140, pp. 1649–1650, 1993.
- [12] F. Halzen and A. D. Martin, “Quarks and leptons,” 1984.
- [13] D. Griffiths, *Introduction to elementary particles*. John Wiley & Sons, 2008.
- [14] M. Tanabashi, P. Richardson, A. Bettini, A. Vogt, L. Garren, A. J. Schwartz, K. Terashi, M. Karliner, R. S. Chivukula, T. Sjöstrand, *et al.*, “Aps: Review of particle physics,” *Phys. Rev. D*, vol. 98, p. 030001, 2018.

- [15] T. K. Gaisser and M. Honda, “Flux of atmospheric neutrinos,” *Annual Review of Nuclear and Particle Science*, vol. 52, no. 1, pp. 153–199, 2002.
- [16] E. Regener and G. Pfotzer, “Vertical intensity of cosmic rays by threefold coincidences in the stratosphere,” *Nature*, vol. 136, no. 3444, p. 718, 1935.
- [17] O. Allkofer, R. Andresen, and W. Dau, “The muon spectra near the geomagnetic equator,” *Canadian Journal of Physics*, vol. 46, no. 10, pp. S301–S305, 1968.
- [18] O. Allkofer, R. Andresen, K. Clausen, and W. Dau, “Sea-level muon spectrum at two different latitudes,” *Journal of Geophysical Research*, vol. 77, no. 22, pp. 4251–4253, 1972.
- [19] C. Augusto, C. Navia, and K. Tsui, “Muon enhancements at sea level in association with swift-bat and milagro triggers,” *Physical Review D*, vol. 77, no. 12, p. 123008, 2008.
- [20] [https://www.nasa.gov/mission\\_pages/station/research/experiments/1043.html](https://www.nasa.gov/mission_pages/station/research/experiments/1043.html), “International space station internal radiation monitoring (iss internal radiation monitoring) - 04.05.17,” Dec 2018.
- [21] T. Dachev, W. Atwell, E. Semones, B. Tomov, and B. Reddell, “Observations of the saa radiation distribution by liulin-e094 instrument on iss,” *Advances in Space Research*, vol. 37, no. 9, pp. 1672–1677, 2006.
- [22] L. Pinsky, W. Osborne, J. Bailey, R. Benson, and L. Thompson, “Light flashes observed by astronauts on apollo 11 through apollo 17,” *Science*, vol. 183, no. 4128, pp. 957–959, 1974.
- [23] C. Fuglesang, L. Narici, P. Picozza, and W. G. Sannita, “Phosphenes in low earth orbit: survey responses from 59 astronauts,” *Aviation, space, and environmental medicine*, vol. 77, no. 4, pp. 449–452, 2006.
- [24] A. Rinaldi, “Phosphenes in space: a study on the interaction between carbon ions and rod photoreceptor,” 2009.
- [25] C. Augusto, C. Navia, H. Shigueoka, K. Tsui, and A. Fauth, “Muon excess at sea level from solar flares in association with the fermi gbm spacecraft detector,” *Physical Review D*, vol. 84, no. 4, p. 042002, 2011.
- [26] M. Savić, D. Maletić, D. Joković, N. Veselinović, R. Banjanac, V. Udovičić, and A. Dragić, “Pressure and temperature effect corrections of atmospheric muon data in the belgrade cosmic-ray station,” in *Journal of Physics: Conference Series*, vol. 632, p. 012059, IOP Publishing, 2015.
- [27] P. H. Barrett, L. M. Bollinger, G. Cocconi, Y. Eisenberg, and K. Greisen, “Interpretation of cosmic-ray measurements far underground,” *Reviews of Modern Physics*, vol. 24, no. 3, p. 133, 1952.
- [28] F. An, A. Balantekin, H. Band, M. Bishai, S. Blyth, D. Cao, G. Cao, J. Cao, Y. Chan, J. Chang, *et al.*, “Seasonal variation of the underground cosmic muon flux observed at daya bay,” *Journal of Cosmology and Astroparticle Physics*, vol. 2018, no. 01, p. 001, 2018.

- [29] A. Bouchta, “Seasonal variation of the muon flux seen by amanda,” in *International Cosmic Ray Conference*, vol. 2, p. 108, 1999.
- [30] M. Ambrosio, R. Antolini, G. Auriemma, R. Baker, A. Baldini, G. Barbarino, B. Barish, G. Battistoni, R. Bellotti, C. Bemporad, *et al.*, “Seasonal variations in the underground muon intensity as seen by macro,” *Astroparticle Physics*, vol. 7, no. 1-2, pp. 109–124, 1997.
- [31] W. Benenson, J. W. Harris, H. Stöcker, and H. Lutz, *Handbook of physics*. Springer Science & Business Media, 2006.
- [32] D. Green, *The physics of particle detectors*, vol. 12. Cambridge University Press, 2000.
- [33] W. Li, M. D. Rodriguez, P. Kluth, M. Lang, N. Medvedev, M. Sorokin, J. Zhang, B. Afra, M. Bender, D. Severin, *et al.*, “Nu clear instrum ents and methods in phy sics research b,” *Nuclear Instruments and Methods in Physics Research B*, vol. 302, pp. 40–47, 2013.
- [34] K. A. Olive *et al.*, “Review of Particle Physics,” *Chin. Phys.*, vol. C38, p. 090001, 2014.
- [35] B. R. Martin, *Nuclear and particle physics: an introduction*. John Wiley & Sons, 2006.
- [36] T. Tabata, R. Ito, and S. Okabe, “An empirical equation for the backscattering coefficient of electrons,” *Nuclear instruments and methods*, vol. 94, no. 3, pp. 509–513, 1971.
- [37] M. J. Berger and S. M. Seltzer, “Stopping powers and ranges of electrons and positions,” tech. rep., NATIONAL STANDARD REFERENCE DATA SYSTEM, 1982.
- [38] [https://www.onsemi.com/pub/Collateral/AND9770\\_D.PDF](https://www.onsemi.com/pub/Collateral/AND9770_D.PDF), “On semiconductor: Introduction to the silicon photomultiplier,” Dec 2018.
- [39] <https://www.sensl.com/downloads/ds/TN>
- [40] A. Pla-Dalmau, A. D. Bross, V. V. Rykalin, and B. M. Wood, “Extruded plastic scintillator for minerva,” in *Nuclear Science Symposium Conference Record, 2005 IEEE*, vol. 3, pp. 1298–1300, IEEE, 2005.
- [41] Eljen. <https://eljentechnology.com/products/plastic-scintillators>, accessed: Oct 2018 2018.
- [42] H. Yang, D. Cao, Z. Qian, X. Zhu, C. Loh, A. Huang, R. Zhang, Y. Yang, Y. Liu, B. Xu, *et al.*, “Light attenuation length of high quality linear alkyl benzene as liquid scintillator solvent for the juno experiment,” *Journal of Instrumentation*, vol. 12, no. 11, p. T11004, 2017.
- [43] D. Beznosko, A. Bross, A. Dyshkant, and P.-D. Rykalin, “Fnal-nicadd extruded scintillator,” in *Nuclear Science Symposium Conference Record, 2004 IEEE*, vol. 2, pp. 790–793, IEEE, 2004.
- [44] D. Horrocks, *Applications of liquid scintillation counting*. Elsevier, 2012.
- [45] I. Ambats, Y. Antipov, A. Sadovski, K. Lang, W. Allison, D. Wall, A. Napier, Y. Lai, R. Heinz, D. Wright, *et al.*, “The minos detectors technical design report,” tech. rep., 1998.

- [46] L. Aliaga, L. Bagby, B. Baldin, A. Baumbaugh, A. Bodek, R. Bradford, W. Brooks, D. Boehnlein, S. Boyd, H. Budd, *et al.*, “Design, calibration, and performance of the minerva detector,” *Nuclear Instruments and Methods in Physics Research Section A: Accelerators, Spectrometers, Detectors and Associated Equipment*, vol. 743, pp. 130–159, 2014.
- [47] S. N. Axani, K. Frankiewicz, and J. M. Conrad, “The cosmicwatch desktop muon detector: a self-contained, pocket sized particle detector,” *Journal of Instrumentation*, vol. 13, no. 03, p. P03019, 2018.
- [48] R. De Mendonca, J.-P. Raulin, E. Echer, V. Makhmutov, and G. Fernandez, “Analysis of atmospheric pressure and temperature effects on cosmic ray measurements,” *Journal of Geophysical Research: Space Physics*, vol. 118, no. 4, pp. 1403–1409, 2013.
- [49] LocalConditions.com. <https://www.localconditions.com/weather-madison-wisconsin/53701/past.php>, accessed: Dec. 2018.
- [50] K. Jourde, D. Gibert, J. Marteau, J. de Bremond d’Ars, S. Gardien, C. Girerd, and J.-C. Ianigro, “Monitoring temporal opacity fluctuations of large structures with muon radiography: a calibration experiment using a water tower,” *Scientific reports*, vol. 6, p. 23054, 2016.
- [51] Flight Aware. <https://flightaware.com/>, Dec. 2017.
- [52] <http://nearspace.pl/>, “Near space conference 2018,” Dec 2018.
- [53] K. Albrecht *et al.* (The IceCube Collaboration), “IceCube - the next generation neutrino telescope at the South Pole,” *Nuclear Physics B-Proceedings Supplements*, vol. 118, pp. 388–395, 2003.